



Science Arts & Métiers (SAM)

is an open access repository that collects the work of Arts et Métiers Institute of Technology researchers and makes it freely available over the web where possible.

This is an author-deposited version published in: <https://sam.ensam.eu>
Handle ID: <http://hdl.handle.net/10985/25067>

To cite this version :

Marco MONTEMURRO, Thibaut RODRIGUEZ, Jerome PAILHES, Paul LE TEXIER - On multi-material topology optimisation problems under inhomogeneous Neumann–Dirichlet boundary conditions - Finite Elements in Analysis and Design - Vol. 214, p.103867 - 2023

Any correspondence concerning this service should be sent to the repository

Administrator : scienceouverte@ensam.eu



On multi-material topology optimisation problems under inhomogeneous Neumann–Dirichlet boundary conditions

Marco Montemurro ^{a,*}, Thibaut Rodriguez ^{a,b}, Jérôme Pailhès ^a, Paul Le Texier ^b

^a Arts et Métiers Institute of Technology, Université de Bordeaux, CNRS, INRA, Bordeaux INP, HESAM Université, I2M UMR 5295, F-33405 Talence, France

^b French Atomic Energy Commission, Route des Gargails, BP 2, Le Barp Cedex, France

ABSTRACT

Keywords:

Topology optimisation
Mixed boundary conditions
Multi-material structures
NURBS hyper-surfaces
Finite element method
Density-based method

This work deals with the topology optimisation of structures made of multiple material phases. The proposed approach is based on non-uniform rational basis spline (NURBS) hyper-surfaces to represent the geometric descriptor related to each material phase composing the continuum, and an improved multiphase material interpolation (MMI) scheme to penalise the stiffness tensor of the structure. In this context, the problem is formulated in the most general case by considering inhomogeneous Neumann–Dirichlet boundary conditions and by highlighting the differences between two different problem formulations. The first one uses the work of applied forces and displacements as cost function and the resulting optimisation problem is not self-adjoint. The second one considers the generalised compliance (related to the total potential energy), and the resulting optimisation problem is self-adjoint. Moreover, the improved MMI scheme proposed here does not require the introduction of artificial filtering techniques to smooth the boundary of the topological descriptors of the material phases composing the structure. The effectiveness of the method is proven on both 2D and 3D problems. Specifically, an extensive campaign of numerical analyses is conducted to investigate the influence of the type of geometric descriptor, of the integer parameters involved in the definition of the NURBS entity, of the type of cost function, of the type of lightness requirement, of the number and type of material phases, of the applied boundary conditions on the optimised topology.

1. Introduction

The integration of multiple materials within a structure has always been a challenge in the design of engineering systems subject to different physical requirements. Indeed, a mechanism may be composed of several materials, each one responding to a peculiar requirement in the context of a multi-field analysis: stiffness, strength, thermal conductivity, electrical insulation, damping capability, etc. Nevertheless, one of the main issues when dealing with design problems of multi-material structures is related to conventional joining techniques, which impose limitations on both the properties and the shape of the assembled materials along the interface as well as on the arrangement of materials within the structure.

The development of modern additive manufacturing (AM) processes for multi-material products not only allows manufacturing complex geometries, but also ensures a proper fabrication of multi-material parts, whether composed of plastic materials [1–3], of metals [4,5], or made by a combination of metallic and plastic materials [6,7]. The potential of manufacturing multi-material structures was anticipated since the end of the 1980s by pioneering works in the field of topology optimisation (TO), like the one based on the homogenisation method [8].

This has oriented the scientific and industrial communities towards the development of suited multi-material interpolation laws in the framework of well-established methods, like density-based TO algorithms making use of different interpolation schemes, as the solid isotropic material with penalisation (SIMP) approach [9–11] or the rational approximation for material properties (RAMP) scheme [12], the level set method (LSM) [13–17], the evolutionary structural optimisation (ESO) [18] and the bi-directional evolutionary structural optimisation (BESO) [19,20] approaches, etc., giving rise to the sub-field of multi-material topology optimisation (MMTO). In this background, the goal of MMTO methods is to simultaneously determine the existence and the optimal distribution of N_m material phases in the design domain. MMTO approaches provide additional freedom in generative design, in terms of properties and arrangement of materials within the structure, provided that the mathematical models used in MMTO algorithms are consistent and correctly formulated.

Among the first approaches presented in the literature to deal with MMTO problems, one can find the so-called multi-material SIMP penalisation scheme presented in [10,21,22]. Nevertheless, as extensively

* Corresponding author.

E-mail addresses: marco.montemurro@ensam.eu, marco.montemurro@u-bordeaux.fr (M. Montemurro).

Acronyms

AM	Additive manufacturing
BK1-2D	First 2D benchmark structure
BK2-2D	Second 2D benchmark structure
BK3D	3D benchmark structure
B-spline	Basis spline
BC	Boundary condition
BESO	Bi-directional evolutionary structural optimisation
CAD	Computer aided design
CNLP	Constrained non-linear programming problem
CP	Control point
DMO	Discrete material optimisation
DOF	Degree of freedom
ESO	evolutionary structural optimisation
FE	Finite element
GCMMA	Globally-convergent method of moving asymptotes
GF	Geometric field
LSM	Level set method
MBB	Messerschmitt Bölkow Blohm
MMTO	Multi-material topology optimisation
N-MMI	NURBS-based multi-material interpolation
NURBS	Non-uniform rational basis spline
R-MMI	Recursive multiphase material interpolation
RAMP	Rational approximation for material properties
SANTO	SIMP and NURBS for topology optimisation
SIMP	Solid isotropic material with penalisation
TF	Topological field
TO	Topology optimisation
TPE	Total potential energy
U-MMI	Uniform multiphase material interpolation
WAFD	Work of applied forces and displacements

discussed in [21,22], the material interpolation scheme of the SIMP approach extended to the case of composite structures made of two material phases (without the presence of the void) or three phases (including the presence of the void) does not satisfy the Hashin-Shtrikman bounds when the pseudo-density field associated to each material phase takes low values or when the penalisation coefficient takes high values. Moreover, if the material phases are characterised by a linear elastic isotropic behaviour with the same Young's modulus, but different values of the Poisson's coefficient, the interpolation scheme based on the classic SIMP approach results in odd pseudo-optimal topologies that cannot be manufactured [10,21,22]. This approach also suffers from a dependency of the optimised topology on the order of the material phases implemented in the multi-material interpolation scheme. Despite these limitations, this method has been used to deal with TO problems involving composite structures made of (at most) three material phases, like those discussed in [23–26].

To overcome the limitations of the SIMP material interpolation scheme in the context of MMTO problems, in [21,27,28] the Hashin-Shtrikman bounds have been directly employed for structures composed, at most, of three materials phases. However, the main issues of this approach are related, on the one hand, to the complexity of the analytical formulae involved in the penalisation law and, on the other hand, to the high number of design variables, making, thus, difficult

the generalisation of the method to the case of structures made of N_m material phases.

To go beyond the limitations related to the approach presented in [21,27,28], Zuo and Saitou [29] introduced the ordered multi-material SIMP approach, which allows defining multiple material phases without introducing new design variables for each material. Particularly, a power law and translation coefficients are introduced in the formulation of the multi-material interpolation scheme used to penalise (through a suitable pseudo-density field) the elastic properties of the structure. A heuristic-based optimality criterion is used to update the design variables. This method is applied only to standard 2D benchmark problems dealing with structural stiffness maximisation subject to a mass constraint under homogeneous boundary conditions (BCs) of the Dirichlet type. Moreover, the interpolation scheme is built in the particular case of isotropic materials having the same Poisson's ratio, which does not ensure the possibility of generalising the method to a more general combination of materials.

Taking inspiration from the discrete material optimisation (DMO) [30,31], originally developed for the optimisation of thin-walled composite structures, in [32,33], a generalisation of the SIMP approach for multi-material structures is proposed by introducing a set of optimisation constraints, which enforces the presence of only one material phase at each point of the continuum. Nevertheless, this approach results in a huge number of constraints, which depends upon the number of optimisation variables describing each material phase: this aspect constitutes the main limitation of the method.

Later, two material interpolation schemes inspired by the DMO have been proposed in [34]: the recursive multiphase material interpolation (R-MMI) and the uniform multiphase material interpolation (U-MMI). These approaches have been applied to standard structural stiffness maximisation problems (under homogeneous BCs of the Dirichlet type) subject to constraints on volume/mass either for each material phase or for the whole structure.

Recently, Gao et al. [35] highlighted some limitations of both R-MMI and U-MMI approaches, i.e., numerical issues in the optimised topologies due to the superposition of materials at the frontier between adjacent material phases, convergence towards non-manufacturable local optima, etc. To overcome such limitations, they proposed a new and efficient interpolation scheme for MMTO problems in the context of isogeometric analysis based on the mathematical formalisms of non-uniform rational basis spline (NURBS) entities: this approach is referred to NURBS-based multi-material interpolation (N-MMI). Particularly, this method makes use of the basis spline (B-spline) entities coupled with the Shepard interpolation [36] to represent the geometric descriptor related to each material phase. It is noteworthy that in the framework of the N-MMI scheme, the notion of geometric descriptor is different from the one of topological descriptor (or topological variable) related to each material phase. Roughly speaking, the former represents the “geometrical support” on which relies the latter. Anyway, it must be pointed out that, despite the use of the acronym NURBS to refer to this interpolation scheme, in [35] only B-spline entities are employed.

It is noteworthy that further material interpolation schemes have been developed in the literature in the framework of the LSM. For instance, in [37], a “colour” LSM was proposed and applied to face different problems including the design of compliant mechanisms [38], stress-related requirements [39], etc. Another approach has been presented in [40] where M level-set functions are used to represent the distribution of $M+1$ material phases into the design space. An extension of such an approach was later proposed in [41], where a dedicated formulation was proposed to efficiently control the length scale of each material phase.

Regardless of the adopted interpolation scheme, the most studied problem in the structural optimisation community, when dealing with structures made of multiple material phases, is certainly the one focusing on the maximisation of the structural stiffness subject to a lightness requirement formulated either in terms of a constraint on the overall

mass/volume of the structure or in terms of multiple constraints on the mass/volume fraction of each material phase. However, in almost all the formulations available in the literature [10,21,22,27–29,32–35] a combination of non-zero Neumann BCs and null Dirichlet BCs is considered. In presence of this type of BCs, the work of applied forces and displacements (WAFD) can be used to quantify the structural stiffness.

As recently discussed in [42] for TO problems of anisotropic continua (mono-material case), the WAFD cannot be used to provide a measure of the structural stiffness in presence of inhomogeneous Dirichlet's BCs. In this background, one of the goals of this work is to clarify the role and the influence of inhomogeneous Neumann–Dirichlet BCs on the problem of maximising the stiffness of multi-material structures subject to design requirements on the mass/volume either of the whole structure or of each material phase. Particularly, the theoretical findings recently presented in [42] are extended to MMTO problems in this study.

Firstly, following the same logic steps presented in [42], the total potential energy (TPE) is introduced as a measure of the structural stiffness; subsequently, the analytical expression of the gradient of the merit function related to the TPE in the case of MMTO problems is derived. In this context, it is shown that, under inhomogeneous Neumann–Dirichlet BCs, the TPE-based formulation is self-adjoint while the WAFD-based formulation is not self-adjoint. To the best of the authors' knowledge, it is the first time that this theoretical result has been analytically derived for MMTO problems.

The numerical framework considered in this study is the one of density-based TO methods reformulated in the context of NURBS hyper-surfaces [43–53]. More precisely, the N-MMI scheme presented in [35] is here improved and integrated in the NURBS-density-based TO algorithm, wherein the pseudo-density field related to each material phase, i.e., the geometric descriptor of the material phase, is described by exploiting the general definition of the NURBS hyper-surface. This aspect constitutes the second fundamental contribution of this paper. Indeed, in [35], only B-spline entities were used to describe the geometric descriptors of the materials composing the continuum and a Shepard interpolation function was introduced to obtain smooth boundary of each material phase as well as a clear separation between material phases. However, the introduction of an artificial filtering technique, like the Shepard interpolation function used in [35], reveals useless when using NURBS hyper-surfaces to represent the geometric descriptors of the material phases composing the structure because the weights can ensure both a smooth boundary for each material phase and a clear separation (i.e., minimisation of the regions showing intermediate values of the pseudo-density fields) between material phases.

Unlike classical density-based MMTO approaches, the NURBS-density-based method separates the geometric descriptor of each material phase from the mesh of the finite element (FE) model. Particularly, if the problem dimension is D , a NURBS hyper-surface of dimension $D+1$ is used as a geometric descriptor of the generic material phase: in this way, purely geometric entities are used to describe the distribution of the material phases inside the design domain, which can be easily exported (through a standard data exchange format) to any computer aided design (CAD) software [54,55]. A further advantage of the NURBS-density-based TO algorithm used in this work is that geometric requirements, like, minimum length-scale, maximum length-scale constraints, overhang angle, etc., can be easily formulated and handled because the analytical expression of the boundary of the topology is available at each iteration of the optimisation process [46,47]. Moreover, some fundamental properties of the NURBS basis functions, like the local support property, can be conveniently exploited to facilitate the optimisation process. Specifically, as discussed in [43,44,46], the local support property results in an implicit and efficient filtering technique, which, on the one hand, reduces/avoids the dependency of the optimised solution upon the mesh of the FE model, whilst, on the

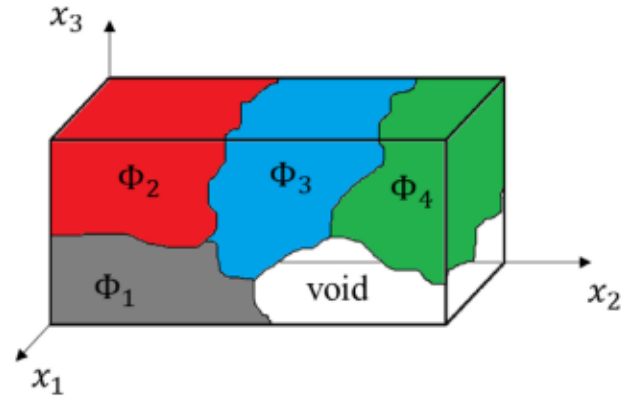


Fig. 1. Schematic representation of the design domain composed of $N_m = 4$ material phases and the void.

other hand, simplifies the calculation of the gradient of the structural responses.

Finally, an extensive campaign of sensitivity analyses is conducted to show the effectiveness of the proposed approach. The first type of sensitivity analysis is conducted to study the influence of the type of entity, i.e., B-spline or NURBS, used as a geometric descriptor of each material phase on the optimised distribution of the materials composing the continuum. Moreover, the effect of the integer parameters of the B-spline/NURBS entity on the optimised solution is also investigated. The second type of sensitivity analysis aims to assess the influence of the number of material phases on the optimised distribution of the material phases. The third one aims to investigate the influence of the inhomogeneous BCs of the Dirichlet type on the solution. The fourth one aims to study the influence of the lightness requirement on the optimised solution; to this end, three formulations are considered: the first one is based on a constraint on the volume fraction of each material phase, the second one is based on a constraint on the total volume fraction of the structure, whilst the last one is based on a constraint on the overall mass fraction of the continuum. The last sensitivity analysis aims to investigate the influence of the problem formulation (WAFD-based or TPE-based) on the optimised topology under inhomogeneous Neumann–Dirichlet BCs.

The paper is structured as follows. The main features of the NURBS-density-based method for MMTO problems are presented in Section 2. The numerical results are provided in Section 3, whilst Section 4 is dedicated to conclusions and prospects of this work.

Notation. Upper-case bold letters and symbols are used to indicate tensors and matrices, while lower-case bold letters and symbols indicate column vectors. $\#S$ denotes the cardinality of the generic set S .

2. The NURBS-density-based topology optimisation method

An exhaustive presentation of the NURBS-density-based method is available in [43,44] (mono-material case). The main features of the method are briefly recalled in the following of this section with a focus on 3D MMTO problems.

2.1. Design variables

Consider the design space $D \subset \mathbb{R}^3$ (a Cartesian orthogonal frame $O(x_1, x_2, x_3)$ is used in the following) composed of N_m material phases and the “void” phase, as schematically illustrated in Fig. 1 in the case $N_m = 4$. The set D can be formally expressed as:

$$D := \{\mathbf{x}^T = (x_1, x_2, x_3) \in \mathbb{R}^3 : x_j \in [0, a_j], j = 1, 2, 3\}, \quad (1)$$

where a_j is the characteristic length of the domain along the x_j axis. In the framework of the N-MMI scheme [35], one must distinguish

between *geometric descriptor* and *topological descriptor* of each material phase. As stated in the introduction, for a 3D problem a 4D NURBS hyper-surface is needed to represent the geometric descriptor of each material phase [44]: the first three coordinates of the NURBS entity associated to the j th material are the Cartesian coordinates defining the design domain, while the fourth one is the geometric field (GF) of the j th material phase, denoted as $\rho_j(\zeta_1, \zeta_2, \zeta_3)$, that reads:

$$\rho_j(\zeta_1, \zeta_2, \zeta_3) := \sum_{i_1=0}^{n_1} \sum_{i_2=0}^{n_2} \sum_{i_3=0}^{n_3} R_{i_1 i_2 i_3}^{(j)}(\zeta_1, \zeta_2, \zeta_3) \rho_{i_1 i_2 i_3}^{(j)}, \quad (2)$$

$$\rho_j \in [0, 1], \quad j = 1, \dots, N_m.$$

In Eq. (2), $\rho_{i_1 i_2 i_3}^{(j)}$ is the value of the GF at the generic control point (CP) of the NURBS hyper-surface, $\zeta_k \in [0, 1]$ is the k th parametric coordinate, and $(n_k + 1)$ is the number of CPs along this direction. The overall number of CPs is $n_{CP} := \prod_{i=1}^3 (n_i + 1)$, while the quantity $R_{i_1 i_2 i_3}^{(j)}$ appearing in Eq. (2) is the generic rational basis function for the j -th material phase that reads:

$$R_{i_1 i_2 i_3}^{(j)} := \frac{\omega_{i_1 i_2 i_3}^{(j)} \prod_{k=1}^3 N_{i_k, p_k}(\zeta_k)}{\sum_{j_1=0}^{n_1} \sum_{j_2=0}^{n_2} \sum_{j_3=0}^{n_3} \left[\omega_{j_1 j_2 j_3}^{(j)} \prod_{k=1}^3 N_{j_k, p_k}(\zeta_k) \right]}, \quad (3)$$

where $N_{i_k, p_k}(\zeta_k)$ are the Bernstein's polynomials of degree p_k [56] and $\omega_{i_1 i_2 i_3}^{(j)}$ are suitable weights that influence the way the NURBS entity is attracted towards a given CP. Of course, in Eq. (2), it is tacitly assumed that the NURBS entities describing the GFs are characterised by the same integer parameters, i.e., number of CPs and degrees of the basis functions, and by the same values of the components of the knot vector along each parametric direction [56]. For more details on the meaning of the different parameters involved in the definition of the NURBS hyper-surface, the interested reader is addressed to [42,44,56].

The dimensionless parameters ζ_j can be defined as:

$$\zeta_j := \frac{x_j}{a_j}, \quad j = 1, 2, 3. \quad (4)$$

The topological field (TF), indicated as $\Phi_j(\zeta_1, \zeta_2, \zeta_3)$, is used to describe the topology of the j th material phase (or, equivalently, its distribution within the design domain) and depends upon a combination of the GFs of all the material phases. In the context of the N-MMI scheme [35], the TF is defined as follows:

$$\Phi_j(\zeta_1, \zeta_2, \zeta_3) := \prod_{k=1}^j \rho_k(\zeta_1, \zeta_2, \zeta_3) \prod_{k=j+1}^{N_m} [1 - \rho_k(\zeta_1, \zeta_2, \zeta_3)], \quad j = 1, \dots, N_m. \quad (5)$$

It is noteworthy that, thanks to the NURBS formalism, the TF of the j th material phase is defined on the dimensionless parametric domain of the NURBS hyper-surface and the information can be correctly passed from this space to the physical one (i.e., the one of the FE analysis, as discussed in the next sub-section) and *vice versa*. Of course, due to the definition provided in Eq. (5), $\Phi_j \in [0, 1]$, ($j = 1, \dots, N_m$).

In this work, unlike the approach presented in [35] where only B-spline entities are used, both the pseudo-density at CPs and the associated weights are considered as design variables and are collected into the vectors ξ_{1j} and ξ_{2j} of the j th material phase, which are defined as:

$$\xi_{1j}^T := (\rho_{000}^{(j)}, \dots, \rho_{n_1 n_2 n_3}^{(j)}), \quad \xi_{2j}^T := (\omega_{000}^{(j)}, \dots, \omega_{n_1 n_2 n_3}^{(j)}), \quad (6)$$

$$\xi_{1j}, \xi_{2j} \in \mathbb{R}^{n_{CP}}, \quad j = 1, \dots, N_m,$$

accordingly, the number of design variables is equal to $n_{var} = k n_{CP} N_m$, where $k = 1$ for B-spline entities and $k = 2$ for NURBS entities. Following the approach presented in [42,44], degrees of the Bernstein's polynomials, knot-vector components and number of CPs, are defined by the user before starting the optimisation process.

In the framework of a deterministic optimisation process, the derivation of the analytical formulae of the gradient of both GF and TF is of

paramount importance. For the sake of compactness of the notation, consider the relationship between the linear index τ and indices i_j , ($j = 1, 2, 3$):

$$\tau := 1 + i_1 + i_2(n_1 + 1) + i_3(n_1 + 1)(n_2 + 1). \quad (7)$$

The partial derivatives of the GF of the j th material reads:

$$\frac{\partial \rho_j(\zeta_1, \zeta_2, \zeta_3)}{\partial \xi_{ik\tau}} = \begin{cases} 0 & \text{if } k \neq j, \quad i = 1, 2, \quad \tau = 1, \dots, n_{CP} \\ R_{\tau}^{(j)}(\zeta_1, \zeta_2, \zeta_3), & \text{if } k = j, \quad i = 1, \quad \tau = 1, \dots, n_{CP} \\ \frac{R_{\tau}^{(j)}(\zeta_1, \zeta_2, \zeta_3)}{\xi_{2j\tau}} [\xi_{1j\tau} - \rho(\zeta_1, \zeta_2, \zeta_3)], & \text{if } k = j, \quad i = 2, \quad \tau = 1, \dots, n_{CP}. \end{cases} \quad (8)$$

Accordingly, the partial derivatives of the TF of the j th material phase can be calculated through the chain rule as follows:

$$\frac{\partial \Phi_j}{\partial \xi_{ik\tau}} = \sum_{s=1}^{N_m} \frac{\partial \Phi_j}{\partial \rho_s} \frac{\partial \rho_s}{\partial \xi_{ik\tau}} = \frac{\partial \Phi_j}{\partial \rho_k} \frac{\partial \rho_k}{\partial \xi_{ik\tau}}, \quad i = 2, \quad k = 1, \dots, N_m, \quad \tau = 1, \dots, n_{CP}, \quad (9)$$

where $\frac{\partial \Phi_j}{\partial \rho_k}$ reads:

$$\frac{\partial \Phi_j}{\partial \rho_k} = \begin{cases} \prod_{q=1}^j \rho_q \prod_{q=j+1}^{N_m} (1 - \rho_q), & \text{if } k \leq j, \\ - \prod_{q=1}^j \rho_q \prod_{q=j+1}^{N_m} (1 - \rho_q), & \text{if } k > j. \end{cases} \quad (10)$$

The implementation of the N-MMI scheme within the NURBS-density-based method has several advantages when compared to R-MMI and U-MMI approaches. Indeed, the following aspects deserve a particular attention.

1. The influence of the design variables of Eq. (6) on the TF of the j th material phase of Eq. (5) is implicit and passes through the definition of the GFs of all material phases, see Eq. (2). This approach avoids the numerical issues related to the explicit dependence of the TF of the j th material phase upon the design variables, as in the case of the DMO methods [34].
2. The expression of the TF of the j th material phase of Eq. (5) avoids overlap between materials at each point of the continuum, without the need of introducing explicit optimisation constraints into the problem formulation, as done in [34].
3. Unlike the approach presented in [35], the N-MMI scheme presented in this study makes use of general NURBS entities by including both the pseudo-density values at each CP and the associated weights into the vector of design variables. As discussed in [42–44], the use of NURBS entities allows obtaining topologies with a boundary smoother than the one of B-spline counterparts. Accordingly, there is no need of introducing a smoothing interpolation function, like the Shepard function used in [35].
4. The TF of the j th material phase of Eq. (5) inherits all the advantages of the NURBS entities used to describe the GFs of Eq. (2): (i) a continuous description of each material phase based on a pure geometric CAD-compatible entity; (ii) the local support property [42,44], which constitutes an implicit filtering scheme that reduces/avoids the dependency of the solution upon the mesh of the FE model.
5. As a consequence of the utilisation of NURBS entities to describe the GF of the j th material phase, the number of design variables is reduced when compared to pure FE-based description of the GFs. Nevertheless, it is still high, mainly for 3D problems involving more than three material phases.

Remark 2.1. Thanks to the properties of NURBS entities [56] and to Eqs. (2) and (5), the TF of the j th material phase can be represented through the standard formula of a NURBS entity. To understand this aspect, consider two distinct NURBS scalar functions in the simplest case $N = 1$:

$$h_s(\zeta) = \frac{1}{a_s(\zeta)} \sum_{i=0}^n N_{i,p}(\zeta) \omega_i^{(s)} y_i^{(s)}, \text{ with } a_s(\zeta) := \sum_{i=0}^n N_{i,p}(\zeta) \omega_i^{(s)}, \quad s = 1, 2. \quad (11)$$

It is easy to prove (this is left as exercise to the reader) that the product of two NURBS functions $h_1 h_2$ can be expressed as follows:

$$\tilde{h}(\zeta) = h_1 h_2 = \frac{1}{\tilde{a}(\zeta)} \sum_{k=1}^{(n+1)^2} \tilde{N}_{k,p}(\zeta) \tilde{\omega}_k \tilde{y}_k, \quad (12)$$

where the relation between index $k = 1, \dots, (n+1)^2$ and indices $i, j = 0, \dots, n$, used for the two NURBS scalar functions reads

$$k = 1 + i + j(n+1). \quad (13)$$

The other quantities appearing in Eq. (12) are defined as follows:

$$\tilde{a}(\zeta) := a_1(\zeta) a_2(\zeta), \quad \tilde{N}_{k,p}(\zeta) := N_{i,p}(\zeta) N_{j,p}(\zeta), \quad \tilde{\omega}_k := \omega_i \omega_j, \quad \tilde{y}_k := y_i y_j. \quad (14)$$

Therefore, also the TF of Eq. (5) can be represented through a combination of CAD-compatible entities, wherein the geometric information along each parametric direction must be updated according to Eqs. (12)–(14).

2.2. Structural responses and objective function definition

Consider the static equilibrium of the FE model in the most general case of inhomogeneous mixed BCs:

$$\hat{\mathbf{K}} \hat{\mathbf{u}} = \hat{\mathbf{f}}, \quad \hat{\mathbf{u}}, \hat{\mathbf{f}} \in \mathbb{R}^{\hat{N}_{\text{DOF}}}, \quad \hat{\mathbf{K}} \in \mathbb{R}^{\hat{N}_{\text{DOF}} \times \hat{N}_{\text{DOF}}}, \quad (15)$$

where \hat{N}_{DOF} , $\hat{\mathbf{K}}$, $\hat{\mathbf{f}}$ and $\hat{\mathbf{u}}$ are the number of degrees of freedom (DOFs), the (singular) stiffness matrix of the structure, the vector of external nodal forces/moments and the vectors of DOFs before the application of BCs.

Definition 2.1. Consider a rectangular matrix $\hat{\mathbf{M}} \in \mathbb{R}^{m \times n}$ and the following sets of positive integers: $\mathcal{R} \subset \{i \mid 1 \leq i \leq m\}$ and $\mathcal{C} \subset \{j \mid 1 \leq j \leq n\}$. The matrix $\hat{\mathbf{M}} := \mathfrak{R}(\hat{\mathbf{M}}, \mathcal{R}, \mathcal{C})$ is obtained by suppressing the i th row and the j th column from $\hat{\mathbf{M}}$, $\forall i \in \mathcal{R}$ and $\forall j \in \mathcal{C}$. Similarly, consider the vector $\hat{\mathbf{v}} \in \mathbb{R}^n$; then $\mathbf{v} := \mathfrak{R}(\hat{\mathbf{v}}, \mathcal{R})$ is the vector that can be obtained by deleting the i th row of $\hat{\mathbf{v}}$, $\forall i \in \mathcal{R}$.

Let $I_U \subset \{i \mid 1 \leq i \leq \hat{N}_{\text{DOF}}\}$ and $I_{\text{BC}} \subset \{i \mid 1 \leq i \leq \hat{N}_{\text{DOF}}\}$ be two generic sets of indices such that: $I_U \cap I_{\text{BC}} = \emptyset$, $\#I_U = N_{\text{DOF}}$, $\#I_{\text{BC}} = N_{\text{BC}}$ and $N_{\text{DOF}} + N_{\text{BC}} = \hat{N}_{\text{DOF}}$ (i.e., N_{BC} is the number of DOFs where generalised displacements are imposed, whilst N_{DOF} is the number of unknown DOFs). When applying Definition 2.1 to Eq. (15), one obtains

$$\begin{bmatrix} \mathbf{K} & \mathbf{K}_{\text{BC}} \\ \mathbf{K}_{\text{BC}}^T & \tilde{\mathbf{K}} \end{bmatrix} \begin{Bmatrix} \mathbf{u} \\ \mathbf{u}_{\text{BC}} \end{Bmatrix} = \begin{Bmatrix} \mathbf{f} \\ \mathbf{r} \end{Bmatrix}, \quad (16)$$

with:

$$\mathbf{u} := \mathfrak{R}(\hat{\mathbf{u}}, I_U), \quad \mathbf{f} := \mathfrak{R}(\hat{\mathbf{f}}, I_U)$$

$$\mathbf{u}_{\text{BC}} := \mathfrak{R}(\hat{\mathbf{u}}, I_{\text{BC}}), \quad \mathbf{r} := \mathfrak{R}(\hat{\mathbf{f}}, I_{\text{BC}}),$$

$$\mathbf{K} := \mathfrak{R}(\hat{\mathbf{K}}, I_{\text{BC}}, I_{\text{BC}}), \quad \mathbf{K}_{\text{BC}} := \mathfrak{R}(\hat{\mathbf{K}}, I_{\text{BC}}, I_U), \quad \tilde{\mathbf{K}} := \mathfrak{R}(\hat{\mathbf{K}}, I_U, I_U), \quad (17)$$

$$\mathbf{u}, \mathbf{f} \in \mathbb{R}^{N_{\text{DOF}}}, \quad \mathbf{u}_{\text{BC}}, \mathbf{r} \in \mathbb{R}^{N_{\text{BC}}},$$

$$\mathbf{K} \in \mathbb{R}^{N_{\text{DOF}} \times N_{\text{DOF}}}, \quad \mathbf{K}_{\text{BC}} \in \mathbb{R}^{N_{\text{DOF}} \times N_{\text{BC}}}, \quad \tilde{\mathbf{K}} \in \mathbb{R}^{N_{\text{BC}} \times N_{\text{BC}}}.$$

In Eq. (16), \mathbf{u} and \mathbf{u}_{BC} are the vectors of unknown and imposed DOFs, respectively, while \mathbf{f} and \mathbf{r} are the vectors of external nodal forces/moments and nodal reactions, respectively. \mathbf{K} , \mathbf{K}_{BC} and $\tilde{\mathbf{K}}$ are the (non-singular) stiffness matrices after applying BCs and reordering DOFs.

In the context of the NURBS-density-based approach, the TFs related to the material phases composing the structure affect the element stiffness matrix and, thus, the global stiffness matrix as:

$$\hat{\mathbf{K}} := \sum_{e=1}^{N_e} \sum_{j=1}^{N_m} \Phi_{je}^{\alpha} \hat{\mathbf{I}}_e^T \mathbf{K}_{je}^0 \hat{\mathbf{I}}_e = \sum_{e=1}^{N_e} \sum_{j=1}^{N_m} \hat{\mathbf{I}}_e^T \mathbf{K}_{je} \hat{\mathbf{I}}_e, \quad (18)$$

$$\mathbf{K}_{je}^0, \mathbf{K}_{je} \in \mathbb{R}^{N_{\text{DOF}}^e \times N_{\text{DOF}}^e}, \quad \hat{\mathbf{I}}_e \in \mathbb{R}^{N_{\text{DOF}}^e \times \hat{N}_{\text{DOF}}},$$

where Φ_{je} is the TF of the j th material phase of Eq. (5) computed at the centroid of the generic element e , whilst $\alpha = 3$ is used to penalise the intermediate values between 0 and 1, as done in the SIMP approach. N_e is the total number of elements and N_{DOF}^e is the number of DOFs of the generic element. In Eq. (18), \mathbf{K}_{je}^0 and \mathbf{K}_{je} are the non-penalised and the penalised stiffness matrices of element e , expressed in the global reference frame of the FE model, whilst $\hat{\mathbf{I}}_e$ is the connectivity matrix of element e defined as:

$$\mathbf{u}_e = \hat{\mathbf{I}}_e \hat{\mathbf{u}}, \quad (19)$$

where $\mathbf{u}_e \in \mathbb{R}^{N_{\text{DOF}}^e}$ is the vector of DOFs of element e .

Remark 2.2. The N-MMI scheme of Eq. (18) satisfies the Hashin–Shtrikman bounds [57]. This can be easily verified by considering the case of $N_m = 2$ materials. In this case, the number of constitutive phases composing the structure is three, i.e., two material phases and the void. According to Eq. (5), the expression of the two TFs is:

$$\Phi_1 = \rho_1 (1 - \rho_2), \quad \Phi_2 = \rho_1 \rho_2. \quad (20)$$

The quantities Φ_1 and Φ_2 in Eq. (20) can be interpreted, from a mechanical standpoint, as the volume fractions of the material phases related to the TFs. Therefore, the volume fraction of the void is $\Phi_0 = 1 - \Phi_1 - \Phi_2$. When looking at Eq. (20), one can immediately understand the difference between GFs and TFs. If, for a given element, $\rho_1 \rightarrow 0$, there is no material, i.e., $\Phi_j \rightarrow 0$, $j = 1, 2$. Accordingly, the GF ρ_1 translates the presence (or absence) of both material phases at a given point of the continuum. If $\rho_2 \rightarrow 0$ and $\rho_1 \neq 0$, only the material phase associated to TF Φ_1 affects the stiffness tensor of the element according to Eq. (18) because $\Phi_2 \rightarrow 0$. Finally, if $\rho_2 \rightarrow 1$ and $\rho_1 \neq 0$, only the material phase associated to TF Φ_2 affects the stiffness tensor of the element because $\Phi_1 \rightarrow 0$.

Consider now the following numerical example. The void is characterised by the following properties: $E_0 \rightarrow 0$ GPa (Young's modulus), $G_0 \rightarrow 0$ GPa (shear modulus), $K_0 \rightarrow 0$ GPa (bulk modulus) and $\nu_0 \rightarrow 0$ (Poisson's coefficient). The material related to TF Φ_1 is characterised by the following properties $E_1 = 70$ GPa, $\nu_1 = 0.33$, $G_1 = \frac{E_1}{2(1+\nu_1)} = 26.32$ GPa, $K_1 = \frac{E_1}{3(1-2\nu_1)} = 68.63$ GPa. The material related to TF Φ_2 is characterised by the following properties $E_2 = 210$ GPa, $\nu_2 = 0.33$, $G_2 = \frac{E_2}{2(1+\nu_2)} = 78.95$ GPa, $K_2 = \frac{E_2}{3(1-2\nu_2)} = 205.88$ GPa. The Hashin–Shtrikman bounds [57] for a three-phase continuum, where K_0 is the bulk modulus of the weakest material (the void) and K_2 is the bulk modulus of the stiffest material (the one related to the TF Φ_2), read:

$$K_{\text{LB}}^{\text{HT}} \rightarrow 0, \quad K_{\text{UB}}^{\text{HT}} := K_2 + \frac{A_2}{1 + \alpha_2 A_2}, \quad (21)$$

where A_2 and α_2 are defined as:

$$\alpha_2 := -\frac{3}{3K_2 + 4G_2}, \quad A_2 := \frac{\Phi_0}{(K_0 - K_2)^{-1} - \alpha_2} + \frac{\Phi_1}{(K_1 - K_2)^{-1} - \alpha_2}. \quad (22)$$

Moreover, it is possible to compare the elastic properties calculated through the N-MMI scheme, for given values of ρ_1 and ρ_2 , also to Reuss–Voigt bounds [57], which, for a continuum composed of two materials

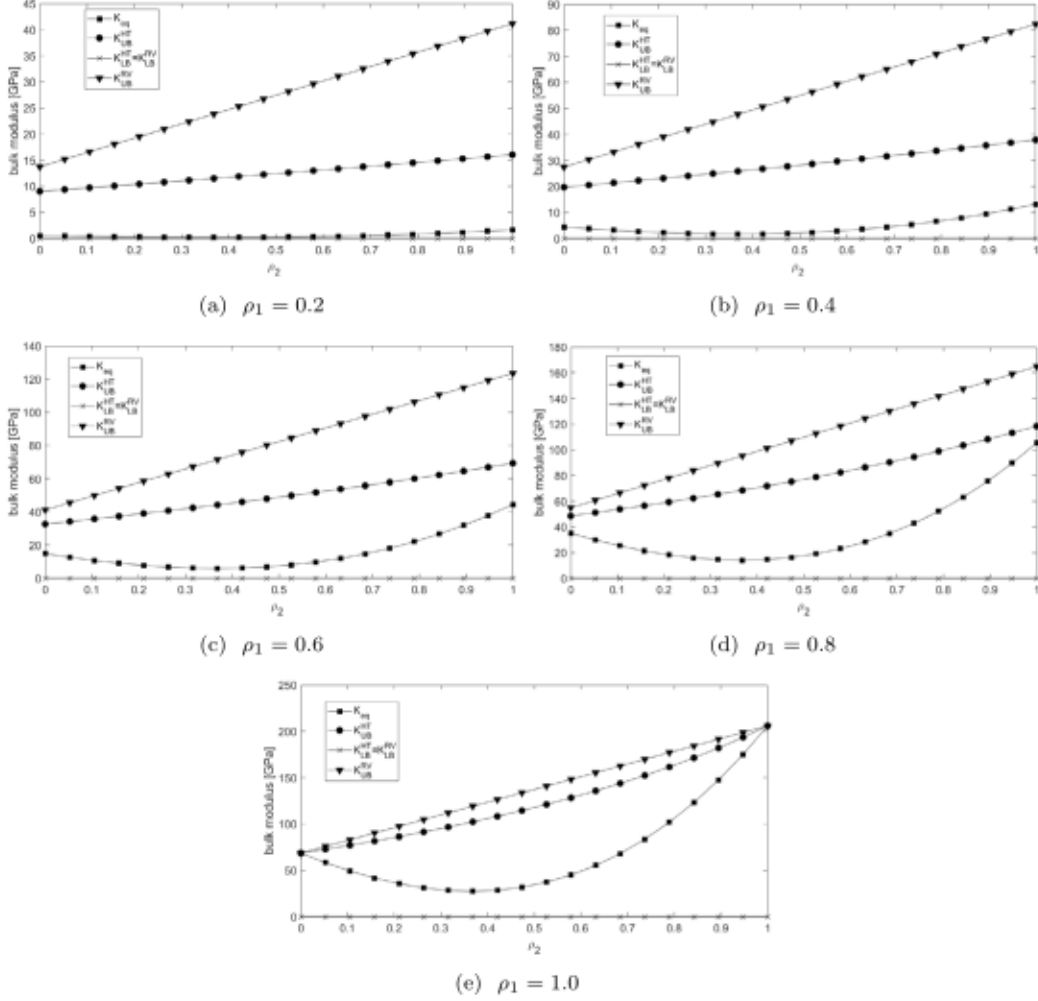


Fig. 2. Equivalent bulk modulus, Reuss-Voigt and Hashin-Shtrikman bounds vs. ρ_1 and ρ_2 in the case $N_m = 2$ material phases.

and the void read:

$$K_{LB}^{RV} \rightarrow 0, \quad K_{UB}^{RV} := \Phi_1 K_1 + \Phi_2 K_2. \quad (23)$$

The trend of the equivalent bulk modulus K_{eq} , which is evaluated through Eq. (18) specialised to the bulk modulus of two isotropic material phases, vs. ρ_2 for five different values of ρ_1 , i.e., $\rho_1 = 0.2, 0.4, 0.6, 0.8, 1.0$, together with the variation of the Hashin-Shtrikman and Reuss-Voigt lower and upper bounds is reported in Fig. 2. As one can infer from the analysis of Fig. 2, for each value of the GF ρ_1 , the equivalent bulk modulus calculated through Eq. (18) falls always between lower and upper bounds (both Hashin-Shtrikman and Reuss-Voigt bounds). Moreover, using a power $\alpha = 3$ in Eq. (18) represents a strong advantage, which consists in enforcing locally, i.e., at each point of the design space, the convergence of the algorithm towards $\rho_1 = 1$ and to preserve just one material phase, i.e., either the material related to TF Φ_1 (when $\rho_2 \rightarrow 0$) or the material associated to TF Φ_2 (when $\rho_2 \rightarrow 1$). Indeed, as one can verify from a quick glance to Fig. 2, when $\rho_1 = 1$, due to the non-monotonicity of the function, the equivalent bulk modulus is strongly penalised with respect to the value of the bulk modulus of each constitutive phase for all $\rho_2 \in]0, 1[$, i.e., all the “physically-meaningless” intermediate values.

The volume of the j th material phase is penalised as follows:

$$V_j(\xi_{11}, \xi_{21}, \dots, \xi_{1N_m}, \xi_{2N_m}) := \sum_{e=1}^{N_e} \Phi_{je} V_e. \quad (24)$$

where V_e is the volume of element e . The overall volume of the structure reads

$$V(\xi_{11}, \xi_{21}, \dots, \xi_{1N_m}, \xi_{2N_m}) := \sum_{j=1}^{N_m} V_j, \quad (25)$$

while the overall mass is expressed as

$$M(\xi_{11}, \xi_{21}, \dots, \xi_{1N_m}, \xi_{2N_m}) := \sum_{j=1}^{N_m} \rho_j V_j, \quad (26)$$

where ρ_j is the density of the j th material phase.

Two types of merit function are considered in this study. The first one is the WAFD which reads:

$$\mathcal{W}(\xi_{11}, \xi_{21}, \dots, \xi_{1N_m}, \xi_{2N_m}) := \mathbf{f}^T \mathbf{u} + \mathbf{u}_{BC}^T \mathbf{r}. \quad (27)$$

The second cost function is the generalised compliance defined in [42], which is related to the TPE Π according to the following formula:

$$C(\xi_{11}, \xi_{21}, \dots, \xi_{1N_m}, \xi_{2N_m}) := -2\Pi(\xi_{11}, \xi_{21}, \dots, \xi_{1N_m}, \xi_{2N_m}), \quad (28)$$

where the TPE is defined as

$$\Pi(\xi_{11}, \xi_{21}, \dots, \xi_{1N_m}, \xi_{2N_m}) := \frac{1}{2} \hat{\mathbf{u}}^T \hat{\mathbf{K}} \hat{\mathbf{u}} - \mathbf{f}^T \mathbf{u}. \quad (29)$$

By combining the above formulae, the generalised compliance simplifies to:

$$C(\xi_{11}, \xi_{21}, \dots, \xi_{1N_m}, \xi_{2N_m}) = \mathbf{f}^T \mathbf{u} - \mathbf{u}_{BC}^T \mathbf{r}. \quad (30)$$

The physical meaning of the generalised compliance is clear: when only pure forces/moments are applied the smaller the resulting displacement/rotations the greater the stiffness of the structure (and thus the smaller the generalised compliance). Conversely, when pure displacements/rotations are applied the higher the reaction forces the higher the structural stiffness and, consequently, the smaller the generalised compliance (which can become negative).

The derivation of the formal expression of the gradient of the structural responses with respect to the design variables is mandatory to speed up the optimisation process when a deterministic algorithm is employed to perform the solution search.

As far as the volume and the mass are concerned, the formal expression of their gradient can be easily derived by differentiating Eqs. (24)–(26):

$$\frac{\partial V_j}{\partial \xi_{ik\tau}} = \sum_{e \in S_{k\tau}} V_e \frac{\partial \Phi_{je}}{\partial \rho_k} \frac{\partial \rho_{ke}}{\partial \xi_{ik\tau}}, \quad i = 1, 2, \quad k = 1, \dots, N_m, \quad \tau = 1, \dots, n_{CP}, \quad (31)$$

$$\frac{\partial V}{\partial \xi_{ik\tau}} = \sum_{j=1}^{N_m} \frac{\partial V_j}{\partial \xi_{ik\tau}}, \quad (32)$$

$$\frac{\partial M}{\partial \xi_{ik\tau}} = \sum_{j=1}^{N_m} \rho_j \frac{\partial V_j}{\partial \xi_{ik\tau}}. \quad (33)$$

Remark 2.3. In Eq. (31), the quantity $S_{k\tau}$ is the discretised version of the local support [42,44] of the NURBS entity describing the GF of the k th material phase, whilst the subscript e used in the scalar fields appearing in Eqs. (31)–(33), i.e., ρ_{ke} and Φ_{je} (and the associated partial derivatives), means that they are evaluated at the element centroid.

The following propositions provide the formal expression of the gradient of the functional involving either the WAFD or the TPE.

Proposition 2.1. Consider a multi-material structure subject to inhomogeneous Neumann–Dirichlet BCs. Under the hypothesis that the imposed loads/displacements do not depend upon the TFs, the gradient of the WAFD reads:

$$\begin{cases} \frac{\partial \mathcal{W}}{\partial \xi_{ik\tau}} = \alpha \sum_{e \in S_{k\tau}} \frac{\partial \rho_{ke}}{\partial \xi_{ik\tau}} (\mathbf{u}_e^T - 2\mathbf{u}_{e0}^T) \mathbf{K}_{ke}^* \mathbf{u}_e, & i = 1, 2, \quad k = 1, \dots, N_m, \\ \tau = 1, \dots, n_{CP}, \\ \mathbf{K} \mathbf{u}_0 = \mathbf{f}, \end{cases} \quad (34)$$

where matrix \mathbf{K}_{ke}^* is defined as

$$\mathbf{K}_{ke}^* := \sum_{j=1}^{N_m} \Phi_{je}^{\alpha-1} \frac{\partial \Phi_{je}}{\partial \rho_k} \mathbf{K}_{je}^0, \quad (35)$$

while \mathbf{u}_{e0} can be obtained from the following formula

$$\mathbf{u}_{e0} = \mathfrak{R}(\hat{\mathbf{L}}_e, \emptyset, \mathbf{I}_{BC}) \mathbf{u}_0 = \mathbf{L}_e \mathbf{u}_0. \quad (36)$$

A proof of Proposition 2.1 is provided in Appendix A.

Remark 2.4. The vector \mathbf{u}_0 appearing in Eq. (34) is the solution of Eq. (16) when $\mathbf{u}_{BC} = \mathbf{0}$.

Remark 2.5. The WAFD is not a self-adjoint functional because, as discussed in Appendix A, to assess its gradient the following adjoint vector must be introduced:

$$\boldsymbol{\eta} = \mathbf{u} - 2\mathbf{u}_0, \quad (37)$$

which depends upon the solution \mathbf{u}_0 of the auxiliary system of Eq. (34). All the details about the adjoint vector $\boldsymbol{\eta}$ are given in Appendix A.

Proposition 2.2. Under the same hypotheses of Proposition 2.1, the gradient of the generalised compliance reads:

$$\frac{\partial C}{\partial \xi_{ik\tau}} = -\alpha \sum_{e \in S_{k\tau}} \frac{\partial \rho_{ke}}{\partial \xi_{ik\tau}} \mathbf{u}_e^T \mathbf{K}_{ke}^* \mathbf{u}_e, \quad i = 1, 2, \quad k = 1, \dots, N_m, \quad \tau = 1, \dots, n_{CP}. \quad (38)$$

A proof of Proposition 2.2 is provided in Appendix B.

2.3. Design requirements and constraint functions definition

Two types of design requirements are considered in this study. The first one is the lightness requirement. It can be integrated in the problem formulation in three different ways. The first way consists of imposing a constraint on the overall mass of the structure as follows:

$$g_M(\xi_{11}, \xi_{21}, \dots, \xi_{1N_m}, \xi_{2N_m}) := \frac{M}{M_{\text{ref}}} - \gamma_M \leq 0, \quad (39)$$

where M_{ref} is a reference value of the mass of the structure, whilst γ_M is the imposed mass fraction.

Alternatively, the lightness requirement can be formulated either in terms of a constraint on the volume of the j th material phase, i.e.,

$$g_{V_j}(\xi_{11}, \xi_{21}, \dots, \xi_{1N_m}, \xi_{2N_m}) := \frac{V_j}{V_{\text{ref}}} - \gamma_{V_j} \leq 0, \quad j = 1, \dots, N_m, \quad (40)$$

or in terms of a constraint on the overall volume of the structure, i.e.,

$$g_V(\xi_{11}, \xi_{21}, \dots, \xi_{1N_m}, \xi_{2N_m}) := \frac{V}{V_{\text{ref}}} - \gamma_V \leq 0. \quad (41)$$

In Eqs. (40) and (41), V_{ref} is a reference value of the volume, whilst γ_{V_j} and γ_V represent the imposed volume fraction for the j th material phase and for the whole structure, respectively.

The second requirement is of technological nature. It deals with the minimum dimension that can be fabricated through the selected manufacturing process and is formulated as minimum length scale requirement for each material phase as:

$$g_{MP_j}(\xi_{11}, \xi_{21}, \dots, \xi_{1N_m}, \xi_{2N_m}) := 1 - \frac{d_{j\min}}{d_{MP}} \leq 0, \quad j = 1, \dots, N_m. \quad (42)$$

In Eq. (42), $d_{j\min}$ is the minimum member size of the TF of the j th material phase, whilst d_{MP} is the minimum manufacturable dimension.

It is noteworthy that one of the main advantages of the NURBS-density-based method is in the handling of the geometric constraints imposed to each TF. Particularly, since the TF associated to the generic material phase is described as a combination of NURBS hyper-surfaces, it is possible to set the integer parameters (i.e., n_{CP} and p_j) to automatically satisfy the minimum length scale requirement, without introducing an explicit optimisation constraint in the problem formulation [46]. Moreover, unlike classical density-based TO methods, the minimum length scale requirement is not related to the size of the elements composing the mesh, but it depends only on the value of the integer parameters involved in the definition of the NURBS entities describing the GFs [46]. Accordingly, an eventual mesh refinement has no impact on the minimum member size of each material phase, but only on the value of the structural responses.

2.4. Problem formulation

Four different problem formulations are considered in this work. Each optimisation problem is stated as a constrained non-linear programming problem (CNLPP). The four CNLPPs read:

$$\begin{aligned} & \min_{\xi_{11}, \xi_{21}, \dots, \xi_{1N_m}, \xi_{2N_m}} \frac{C(\xi_{11}, \xi_{21}, \dots, \xi_{1N_m}, \xi_{2N_m})}{|C_{\text{ref}}|}, \\ & \text{subject to :} \\ & \begin{cases} \hat{\mathbf{K}} \hat{\mathbf{u}} = \hat{\mathbf{f}}, \\ g_{V_j}(\xi_{11}, \xi_{21}, \dots, \xi_{1N_m}, \xi_{2N_m}) \leq 0, \\ \xi_{1j\tau} \in [\rho_{\min}, \rho_{\max}], \quad \xi_{2j\tau} \in [\omega_{\min}, \omega_{\max}], \\ j = 1, \dots, N_m, \quad \tau = 1, \dots, n_{CP}. \end{cases} \end{aligned} \quad (43)$$

$$\min_{\xi_{11}, \xi_{21}, \dots, \xi_{1N_m}, \xi_{2N_m}} \frac{C(\xi_{11}, \xi_{21}, \dots, \xi_{1N_m}, \xi_{2N_m})}{|C_{ref}|},$$

subject to :

$$\begin{cases} \hat{\mathbf{K}}\hat{\mathbf{u}} = \hat{\mathbf{f}}, \\ g_V(\xi_{11}, \xi_{21}, \dots, \xi_{1N_m}, \xi_{2N_m}) \leq 0, \\ \xi_{1j\tau} \in [\rho_{min}, \rho_{max}], \quad \xi_{2j\tau} \in [\omega_{min}, \omega_{max}], \\ j = 1, \dots, N_m, \quad \tau = 1, \dots, n_{CP}. \end{cases} \quad (44)$$

$$\min_{\xi_{11}, \xi_{21}, \dots, \xi_{1N_m}, \xi_{2N_m}} \frac{C(\xi_{11}, \xi_{21}, \dots, \xi_{1N_m}, \xi_{2N_m})}{|C_{ref}|},$$

subject to :

$$\begin{cases} \hat{\mathbf{K}}\hat{\mathbf{u}} = \hat{\mathbf{f}}, \\ g_M(\xi_{11}, \xi_{21}, \dots, \xi_{1N_m}, \xi_{2N_m}) \leq 0, \\ \xi_{1j\tau} \in [\rho_{min}, \rho_{max}], \quad \xi_{2j\tau} \in [\omega_{min}, \omega_{max}], \\ j = 1, \dots, N_m, \quad \tau = 1, \dots, n_{CP}. \end{cases} \quad (45)$$

$$\min_{\xi_{11}, \xi_{21}, \dots, \xi_{1N_m}, \xi_{2N_m}} \frac{\mathcal{W}(\xi_{11}, \xi_{21}, \dots, \xi_{1N_m}, \xi_{2N_m})}{\mathcal{W}_{ref}},$$

subject to :

$$\begin{cases} \hat{\mathbf{K}}\hat{\mathbf{u}} = \hat{\mathbf{f}}, \\ g_V(\xi_{11}, \xi_{21}, \dots, \xi_{1N_m}, \xi_{2N_m}) \leq 0, \\ \xi_{1j\tau} \in [\rho_{min}, \rho_{max}], \quad \xi_{2j\tau} \in [\omega_{min}, \omega_{max}], \\ j = 1, \dots, N_m, \quad \tau = 1, \dots, n_{CP}. \end{cases} \quad (46)$$

In Eqs. (43)–(46), C_{ref} and \mathcal{W}_{ref} are the reference values of the generalised compliance and of the WAFD, respectively. It is noteworthy that, since the generalised compliance can take negative values, the absolute value of the reference compliance is considered to get a dimensionless merit function in Eqs. (43)–(45). In Eqs. (43)–(46), ρ_{min} and ρ_{max} are lower and upper bounds of the pseudo-density at each CP, and ω_{min} and ω_{max} are the bounds on the weights (for each GF). Of course, $\rho_{min} > 0$ to avoid the occurrence of singularity during the resolution of the equilibrium problem.

3. Numerical results

The effectiveness of the approach presented in this work is illustrated on 2D and 3D benchmark structures. For each case, both the GF and the TF related to each material phase are shown.

Remark 3.1. All the analyses presented in this study have been performed by considering, at most, $N_m = 3$ material phases. When illustrating the optimised distribution of each material phase, the TFs related to the first, second and third material, i.e., Φ_1 , Φ_2 , Φ_3 , are represented in red, green and blue colours, respectively.

The code SANTO (SIMP and NURBS for topology optimisation) developed at the I2M laboratory in Bordeaux [42–44] is used to carry out all the analyses presented in this section. SANTO is coded in Python[®] environment and can be interfaced with any FE code. In this study, the software ANSYS[®] is used to build the FE model of each benchmark structure and to evaluate the structural responses.

The globally-convergent method of moving asymptotes (GCMMA) algorithm [58] is employed as optimisation solver for the resolution of the CNLPPs of Eqs. (43)–(46). The parameters governing the behaviour of the GCMMA algorithm are reported in Table 1.

Table 1
GCMMA algorithm parameters.

Parameter	Value
move	0.1
albepa	0.1
Stop criterion	Value
Maximum n. of function evaluations	$100n_{var}$
Maximum n. of iterations*	N_{iter}^{max}
Tolerance on objective function	10^{-6}
Tolerance on constraints	10^{-6}
Tolerance on input variables change	10^{-6}
Tolerance on Karush–Kuhn–Tucker norm	10^{-6}

*The value of N_{iter}^{max} depends upon the considered problem.

Table 2
Young's modulus, Poisson's coefficient and density of the isotropic materials used in this study.

ID	E [MPa]	ν	ρ [kg/mm ³]
M1	210 000	0.33	7.8×10^{-6}
M2	70 000	0.33	2.7×10^{-6}
M3	135 000	0.33	4.5×10^{-6}
M4	1	0.3	1.0
M5	0.5	0.3	0.3

Table 3
Elastic properties and density of the transversely isotropic material used in this study.

ID	Young's moduli [GPa]	Shear moduli [GPa]	Poisson's ratios	Density [kg/m ³]
M6	$E_1 = 181$ $E_2 = E_3 = 10.30$	$G_{23} = 3.78$ $G_{13} = G_{12} = 7.17$	$\nu_{23} = 0.42$ $\nu_{13} = \nu_{12} = 0.27$	$\rho = 1760$

Regarding numerical tests, the sensitivity of the optimised distribution of the N_{mat} materials within the design domain to the following aspects is investigated:

1. The type of geometric entity, i.e., B-spline or NURBS, used to describe the GF of each material phase (only for 2D problems);
2. The number of CPs and the degrees of Bernstein's polynomials governing the shape of the B-spline/NURBS entity (only for 2D problems);
3. The type of BC applied to the continuum (only for 2D problems);
4. The number of material phases and the type of the elastic symmetry of each material (for both 2D and 3D problems);
5. The type of optimisation constraint translating the lightness requirement (only for 2D problems for the sake of brevity).

The material properties of the different materials used in the benchmark structures (both 2D and 3D cases) are listed in Tables 2 (isotropic materials) and 3 (transversely isotropic material).

Remark 3.2. Depending on the problem formulation the mass and the WAFD or the generalised compliance of the starting guess are used as a reference values, i.e., M_{ref} , \mathcal{W}_{ref} and C_{ref} to obtain dimensionless quantities. Conversely, for each analysis the reference volume V_{ref} is always the volume of the design space of dimension $D = 2, 3$.

Remark 3.3. For each CNLPP, lower and upper bounds of design variables are set as: $\rho_{min} = 10^{-3}$, $\rho_{max} = 1$; $\omega_{min} = 0.5$, $\omega_{max} = 10$. The non-trivial components of the knot-vectors are uniformly distributed in the interval $[0, 1]$ [42,44].

Remark 3.4. All the calculations are performed on a work-station with an Intel Xeon E5-2697v2 processor (2.70–3.50 GHz) and four cores dedicated to the FE analyses. Of course, the 3D TO problems needed the highest amount of computational resources for an overall time of about 1 h to find a local feasible minimiser.

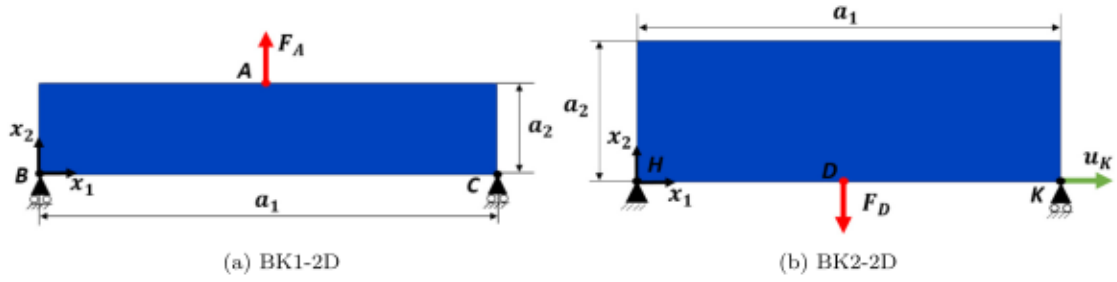


Fig. 3. Geometry and BCs of benchmark structures (a) BK1-2D and (b) BK2-2D.

3.1. 2D benchmark structures

The first 2D benchmark structure (BK1-2D), taken from [59], is a 2D rectangular plate submitted to null BCs of the Dirichlet type, as illustrated in Fig. 3(a). The dimensions of the rectangular domain are: $a_1 = 1000$ mm and $a_2 = 200$ mm. The number of PLANE182 elements (i.e., plane elements, with four nodes and two DOFs per node, plane stress hypothesis with unit thickness) composing the FE model is $N_e = 200 \times 40$. The BCs applied to the structure are:

- $u_2 = 0$ for nodes B and C located at $(x_1, x_2) = (0, 0)$ and $(x_1, x_2) = (a_1, 0)$, respectively;
- $u_1 = 0$ and $F_A = 1000$ N (along the x_2 axis) are applied on node A located at $(x_1, x_2) = (0, a_2)$.

The second 2D benchmark structure (BK2-2D), taken from [42], is the well-known Messerschmitt Bölkow Blohm (MBB) 2D beam submitted to inhomogeneous Neumann–Dirichlet BCs, as illustrated in Fig. 3(b). The dimension of the rectangular design space are: $a_1 = 300$ mm and $a_2 = 100$ mm. The mesh of the FE model is made of $N_e = 120 \times 40$ PLANE182 elements (same hypotheses as in the case of BK1-2D). The applied BCs are:

- $u_1 = u_2 = 0$ for node H located at $(x_1, x_2) = (0, 0)$;
- $u_1 = u_K$, $u_2 = 0$ for node K located at $(x_1, x_2) = (a_1, 0)$; $u_K \in [-30, 30]$ mm with a step of 10 mm;
- $F_D = -1$ N (along the x_2 axis) is applied on node D located at $(x_1, x_2) = (a_1/2, 0)$.

3.1.1. BK1-2D: sensitivity of the optimised topology to the integer parameters of the geometric field descriptor for a bi-material structure

The goal of the numerical analyses conducted on BK1-2D is to investigate both the influence of the type of entity used to represent the GF of each material phase, i.e., B-spline or NURBS, and the effect of the integer parameters (i.e., number of CPs and degrees of the Bernstein's polynomials) involved in its definition on the optimised distribution of the material phases within the design domain. These analyses are carried out only for the CNLPP of Eq. (43), by considering a structure composed of materials M1 and M2 listed in Table 2. The volume fraction of materials M1 and M2 is set to $\gamma_{V1} = 0.3$ and $\gamma_{V2} = 0.15$, respectively.

The following combinations of values of number of CPs and degrees of Bernstein's polynomials have been selected: $n_{CP} = 100 \times 20$, 140×28 , 176×34 , $p_1 = p_2 = 2, 3, 4$. Inasmuch as $\mathbf{u}_{BC} = \mathbf{0}$ for BK1-2D, the generalised compliance and the WAFD are equal. An initial guess characterised by a uniform GF for both material phases, i.e., $\rho_j(\zeta_1, \zeta_2) = \hat{\rho}_j$, $j = 1, \dots, N_m$, has been considered for each analysis. The value of $\hat{\rho}_j$ for the j th material phase is the result of an iterative procedure conducted before the optimisation process: it is calculated to meet the requirement on the volume fraction of the j th TF, i.e., $\Phi_j(\zeta_1, \zeta_2) = \gamma_{Vj}$ ($j = 1, 2$). The reference value of the generalised compliance and of the volume are $C_{ref} = 7684.7$ Nmm and $V_{ref} = a_1 a_2$, whilst the maximum number of iterations is $N_{iter}^{max} = 100$.

Results are provided in terms of dimensionless generalised compliance $\frac{C}{C_{ref}}$ for the different optimised topologies composed of materials M1 (red) and M2 (green) in Figs. 4 and 5, for B-spline and NURBS solutions, respectively. For all these solutions the GCMMA algorithm stopped when the criterion on the maximum number of iterations is met. Specifically, the optimised multi-material topologies illustrated in these figures are the ones obtained after the threshold operation executed on the TF of each material phase to satisfy the optimisation constraints of the problem at hand. Moreover, the TF related to material M1 is illustrated in Figs. 6 and 7, for B-spline and NURBS solutions, respectively, whilst the one related to M2 is shown in Figs. 8 and 9, for B-spline and NURBS solutions, respectively.

From the analysis of the results illustrated in Figs. 4–9 the following remarks can be drawn.

1. In agreement with the results presented in [43,44] for mono-material TO problems, regardless of the type of entity used to describe the GF of the j th material phase, the greater the number of CPs or the smaller the degrees the lower the objective function value.
2. As discussed in [43,44], the optimised topology does not depend upon the mesh quality, but depends on the integer parameters involved in the definition of the GF of each material phase, i.e., B-spline or NURBS entity. Specifically, the number of CPs and the basis functions degrees affect the size of the local support [42,44]. As explained in [46], the local support constitutes a sort of implicit filter, which enforces a minimum length scale in the GFs, which is, thus, transferred to the TF of each material phase. Particularly, the higher the degree or the smaller the number of CPs the larger the local support, thus each CP affects a higher number of elements of the mesh during optimisation. As a consequence, the higher the degree the smoother the boundary of the material phases after CAD reconstruction.
3. Optimised configurations obtained using NURBS surfaces to describe the GFs are characterised by values of the objective function lower than or equal to those related to optimised topologies obtained when B-spline surfaces are used to describe the GFs. Furthermore, from the analysis of Figs. 4 and 5, one can notice that NURBS topologies have a boundary smoother than the one of B-spline solutions.
4. Consider the optimised solutions illustrated in Figs. 4(c) and 5(a) that have been obtained by employing B-spline and NURBS entities, respectively, with the same degree of the Bernstein's polynomials. Particularly, for the solution illustrated in Fig. 4(c) (B-spline case), the number of design variables is $n_{var} = N_m \times n_{CP} = 2 \times 176 \times 34 = 11968$, whilst for the solution illustrated in Fig. 5(a) (NURBS case), the number of design variables is $n_{var} = N_m \times 2n_{CP} = 2 \times 2 \times 100 \times 20 = 8000$. The value of the cost function is 0.0586 and 0.0576 for Figs. 4(c) and 5(a), respectively. Therefore, although the B-spline solution is characterised by a number of design variables greater than that of the NURBS solution, the cost function of the latter is lower

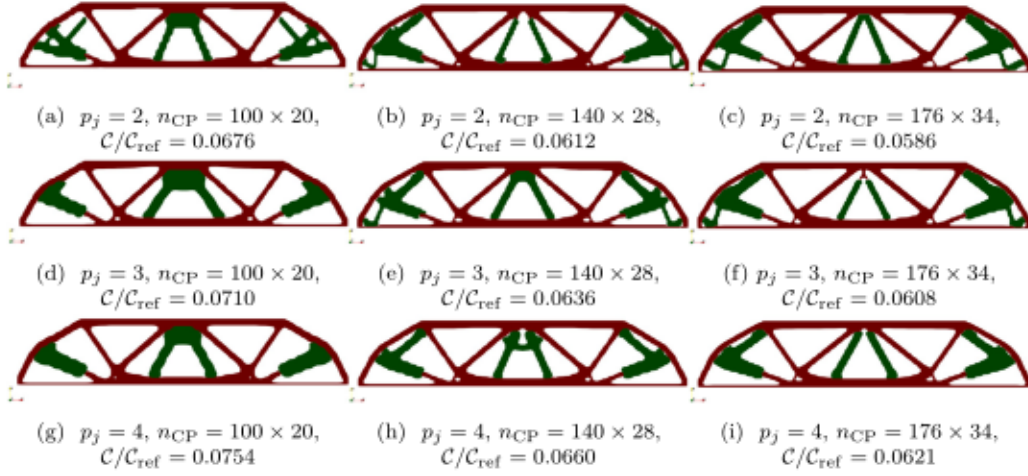


Fig. 4. BK1-2D: optimised solution vs. number of CPs and basis functions degrees, B-spline solutions of problem (43) when considering $N_m = 2$ material phases.

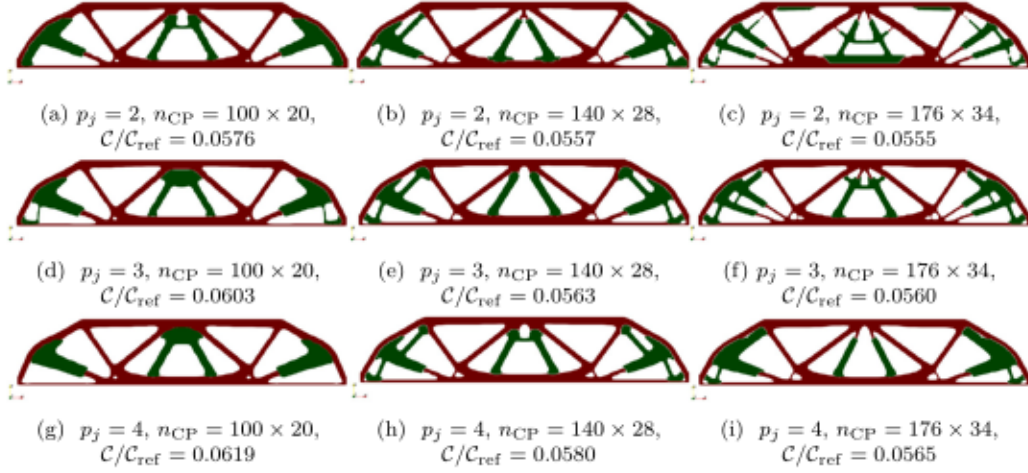


Fig. 5. BK1-2D: optimised solution vs. number of CPs and basis functions degrees, NURBS solutions of problem (43) when considering $N_m = 2$ material phases.

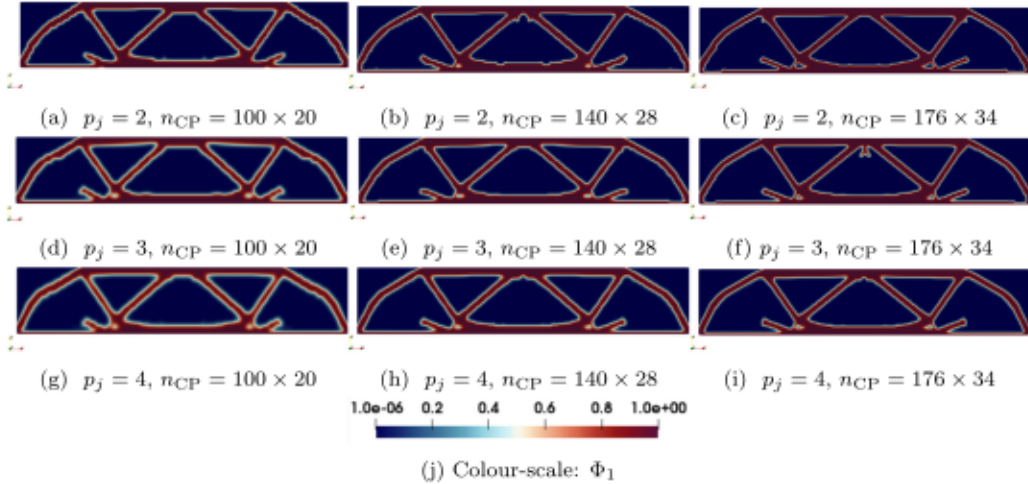


Fig. 6. BK1-2D: sensitivity of the TF Φ_1 to the number of CPs and basis functions degrees, B-spline solutions of problem (43) when considering $N_m = 2$ material phases.

than that of the former. Of course, this remark holds also for B-spline and NURBS solutions characterised by the same number of design variables (which can be obtained by selecting the number of CPs of the B-spline entity in such a way to obtain the same number of design variables associated to the NURBS

entity). Accordingly, for single-scale multi-material TO problems involving stiffness-related and lightness-related requirements the following guideline can be drawn: among B-spline-based solutions and NURBS-based solutions characterised by the same degrees of the Bernstein's polynomials and the same number

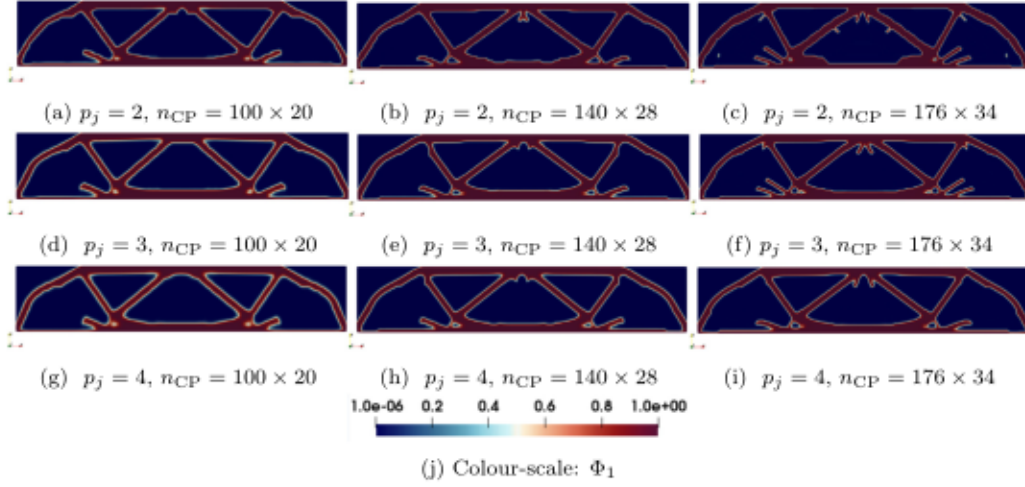


Fig. 7. BK1-2D: sensitivity of the TF Φ_1 to the number of CPs and basis functions degrees, NURBS solutions of problem (43) when considering $N_m = 2$ material phases.

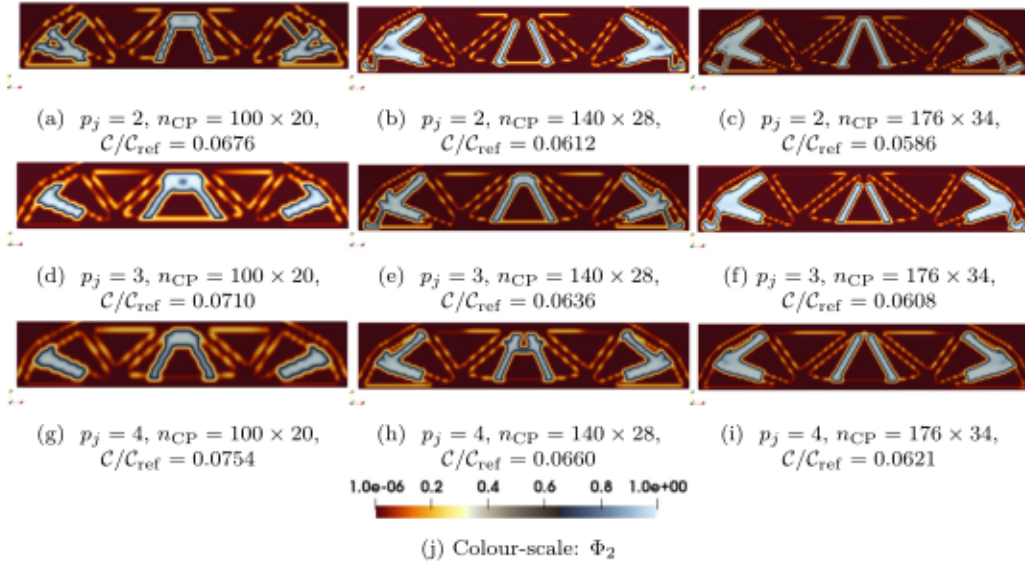


Fig. 8. BK1-2D: sensitivity of the TF Φ_2 to the number of CPs and basis functions degrees, B-spline solutions of problem (43) when considering $N_m = 2$ material phases.

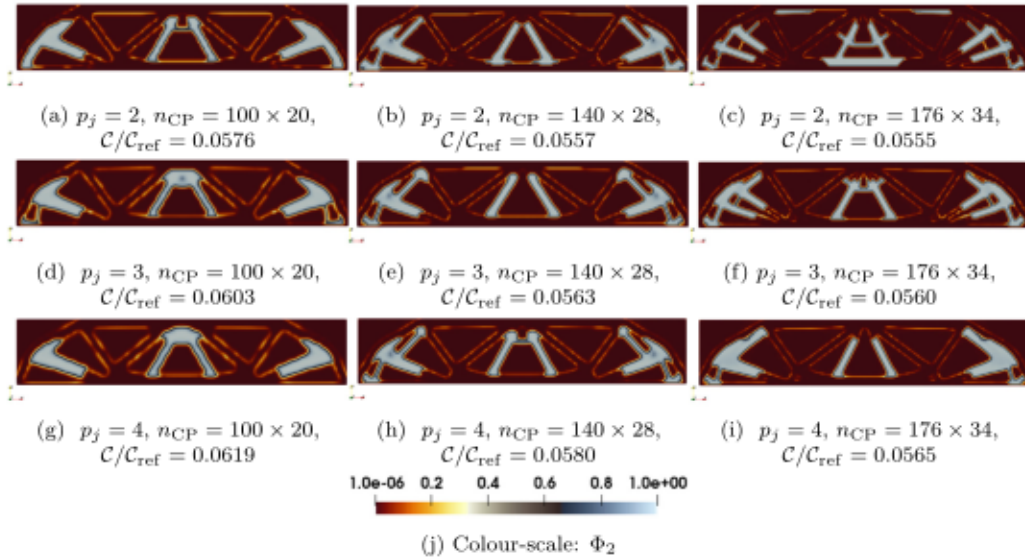


Fig. 9. BK1-2D: sensitivity of the TF Φ_2 to the number of CPs and basis functions degrees, NURBS solutions of problem (43) when considering $N_m = 2$ material phases.

of design variables, the user should always privilege the use of NURBS entities.

- Regardless of the type of entity used to describe each GF, one can notice that the frontier between the TFs describing the material phases M1 and M2 are clearly defined and no overlap among them occurs. Particularly, it is noteworthy that after $N_{iter}^{max} = 100$ iterations the topological descriptor of the first material phase, i.e., Φ_1 , presents a clear point-wise convergence either towards 1 or towards ρ_{min}^2 (see Figs. 6 and 7), unlike the topological descriptor of the second material phase, i.e., Φ_2 , which is characterised by intermediate values circumscribed to very limited zones at the frontier with Φ_1 (as shown in Figs. 8 and 9, the phenomenon is more pronounced for B-spline solutions and it is negligible for NURBS solutions). Of course, as shown in the next subsection, when increasing the maximum number of iterations all the TFs converge towards a clear “black and white” design.

3.1.2. BK1-2D: application to a structure composed of three material phases

The CNLPP of Eq. (43) has been solved for BK1-2D by considering a structure composed of $N_m = 3$ material phases. The material properties used in this case are those of materials M1, M2 and M3 listed in Table 2. Specifically, the TFs Φ_1 , Φ_2 and Φ_3 are associated to materials M1, M2, and M3, respectively. The volume fraction of materials M1, M2 and M3 is set to $\gamma_{V_1} = 0.2$, $\gamma_{V_2} = 0.15$ and $\gamma_{V_3} = 0.1$, respectively.

The minimum dimension characterising the considered manufacturing process, appearing in Eq. (42), is set to $d_{MP} = 7$ mm. Following the approach based on design *abaci* presented in [46], this requirement can be fulfilled by selecting a pertinent number of CPs and degrees of the Bernstein's polynomials. To this end, two cases are considered. In the first one, a B-spline entity characterised by the following values of number of CPs and degrees of Bernstein's polynomials is used to describe the GFs: $n_{CP} = 176 \times 34$, $p_1 = p_2 = 2$. In the second case, a NURBS entity with $n_{CP} = 176 \times 34$ and $p_1 = p_2 = 4$ is used to describe the GFs. Both choices satisfy the constraint on the minimum length scale of Eq. (42).

Since $\mathbf{u}_{BC} = \mathbf{0}$, the generalised compliance and the WAFD coincide (thus the generalised compliance is a non-negative functional in this case). An initial guess characterised by a uniform GF for each material phase, i.e., $\rho_j(\xi_1, \xi_2) = \hat{\rho}_j$, $j = 1, \dots, N_m$, has been considered for each analysis. The value of $\hat{\rho}_j$ for the j th material phase is the result of an iterative procedure conducted before the optimisation process: it is calculated to meet the requirement on the volume fraction of the j th TF, i.e., $\Phi_j(\xi_1, \xi_2) = \gamma_{V_j}$ ($j = 1, 2$). The reference value of the generalised compliance and of the volume are $C_{ref} = 21932.4$ Nmm and $V_{ref} = a_1 a_2$, whilst the maximum number of iterations is $N_{iter}^{max} = 500$.

Results are provided in Fig. 10 in terms of the colour map of the TF Φ_j ($j = 1, \dots, N_m$) related to each material phase, of the optimised topology, of the related dimensionless generalised compliance $\frac{C}{C_{ref}}$ and of the number of iterations N_{iter} when the convergence is achieved for both B-spline and NURBS solutions. It is noteworthy that, for each case, the GCMMA algorithm stopped when the criterion on the difference between the objective function values of two consecutive iterations is met. Moreover, the optimised multi-material topologies illustrated in Figs. 10(j) and 10(k) are obtained by performing the threshold operation on the TF of each material phase (the threshold value is calculated to satisfy the optimisation constraints of the problem at hand): M1, M2 and M3 are indicated in red, green and blue colours, respectively.

The following remarks can be drawn from the analysis of these results.

- In agreement with the results presented in the case of $N_m = 2$ material phases, when NURBS entities are used to describe the GFs, the resulting optimised topology is characterised by a merit function lower than the one of the B-spline counterpart. Moreover, as one can notice from a quick glance to Figs. 10(j)

Table 4

BK2-2D: reference value of the generalised compliance for different values of u_K .

u_K [mm]	-30	-20	-10	0	10	20	30
C_{ref} [Nmm]	418.316	427.378	436.256	444.951	453.462	461.789	469.932

and 10(k), the boundary of NURBS solution is smoother than the one of B-spline solution.

- Thanks to the local support property [42,44] and according to the strategy presented in [46], the choice of the integer parameters involved in the definition of the GF of each material phase results in a minimum length scale equal to or greater than 10 mm. The manufacturing constraint of Eq. (42) is, thus, satisfied without introducing an explicit optimisation constraint in the problem formulation.
- When either a B-spline entity or a NURBS entity is used to describe each GF, the boundary between the TFs describing the material phases M1, M2 and M3 are clearly defined and no overlap occurs. Particularly, it is noteworthy that the topological descriptor of each material phase, i.e., Φ_j ($j = 1, \dots, N_m$), presents a clear point-wise convergence either towards 1 or towards ρ_{min}^3 , as shown in Fig. 10. The convergence is achieved after 281 iterations for the B-spline solution and after 229 iterations for the NURBS solution.

3.1.3. BK2-2D: compliance minimisation under inhomogeneous Neumann-Dirichlet boundary conditions for bi-material structures

The first goal of the numerical analyses conducted on the benchmark structure BK2-2D is to study the influence of the inhomogeneous Neumann-Dirichlet BCs on the optimised distribution of the material phases for a continuum composed of two materials when the generalised compliance is considered as a merit function. Particularly, the material properties of materials M4 and M5 from Table 2 are used in all the analyses described in the followings.

The second goal of this campaign of numerical analyses is to investigate the influence of the problem formulation on the optimised distribution of materials M4 and M5 within the design domain. To this purpose, problems (43), (44) and (45) are solved here by considering a technological constraint related to the minimum fabricable dimension equal to $d_{MP} = 7$ mm (see Eq. (42)). According to the methodology presented in [46], this requirement can be satisfied by choosing a NURBS entity with the following integer parameters: $p_1 = p_2 = 4$ and $n_{CP} = 106 \times 34$. Moreover, for problem (43), the volume fraction of materials M4 and M5 is set to $\gamma_{V_1} = 0.25$ and $\gamma_{V_2} = 0.15$, respectively; for problem (44), the overall volume fraction is set to $\gamma_V = 0.4$; for problem (45), the mass fraction of the structure is set to $\gamma_M = 0.4$.

Since $\mathbf{u}_{BC} \neq \mathbf{0}$ for BK2-2D, the generalised compliance can take negative values. For each problem formulation, an initial guess characterised by a uniform GF for both material phases, i.e., $\rho_j(\xi_1, \xi_2) = \hat{\rho}_j$, $j = 1, \dots, N_m$, has been considered for each analysis. Nevertheless, the value of $\hat{\rho}_j$ for the j th material phase is the result of an iterative procedure conducted before the optimisation process that depends upon the problem formulation. Specifically, the value of $\hat{\rho}_j$ is calculated to meet: (a) the requirement on the volume fraction of the j th TF, i.e., $\Phi_j(\xi_1, \xi_2) = \gamma_{V_j}$ ($j = 1, 2$) for problem (43); (b) the requirement on the total volume fraction for problem (44); (c) the requirement on the total mass fraction for problem (45).

Of course, the reference value of the generalised compliance C_{ref} depends upon the set of applied BCs and is reported in Table 4 for the different values of the applied displacement u_K . The reference volume appearing in the CNLPP of Eqs. (43) and (44) is $V_{ref} = a_1 a_2$, whilst the reference mass used in the CNLPP of Eq. (45) is $M_{ref} = \rho_4 V_{ref}$. For each analysis the maximum number of iterations is $N_{iter}^{max} = 500$.

The optimised distribution of materials M4 (red colour) and M5 (green colour) solutions of problems (43), (44) and (45) are illustrated

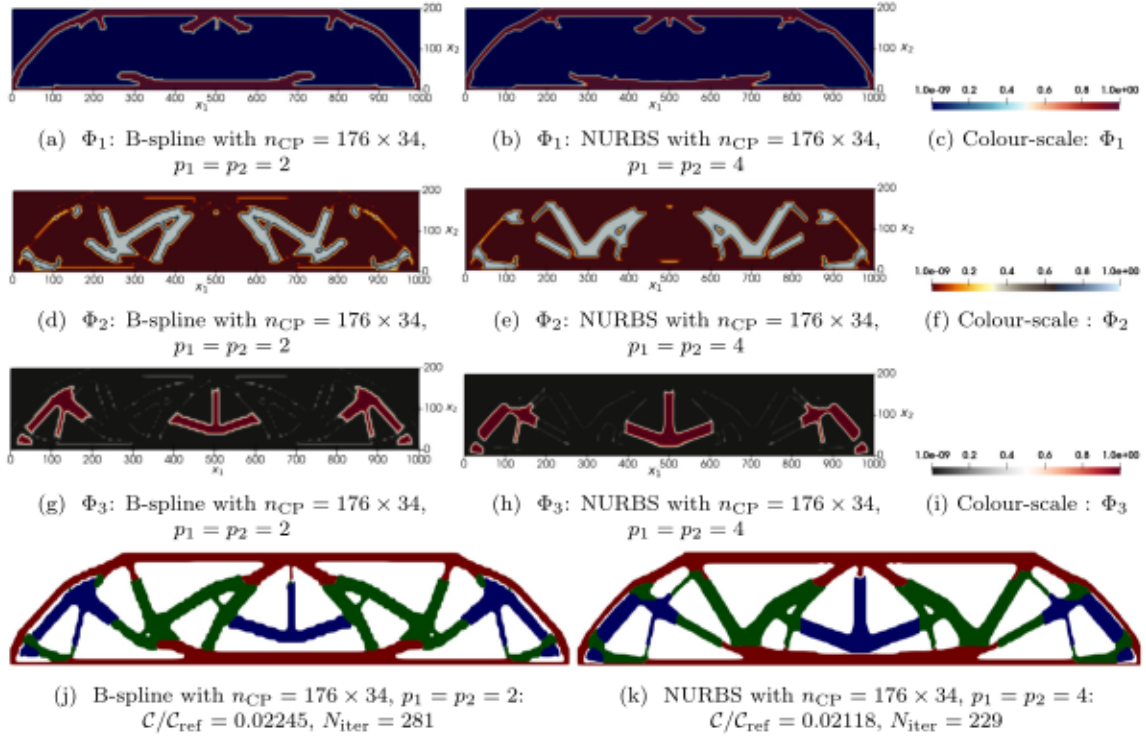


Fig. 10. BK1-2D: Optimised distribution of Φ_1 (M1) (a) and (b), Φ_2 (M2) (d) and (e), Φ_3 (M3) (g) and (h) and optimised topologies (j) and (k) for B-spline and NURBS solutions of problem (43) when considering $N_m = 3$ material phases.

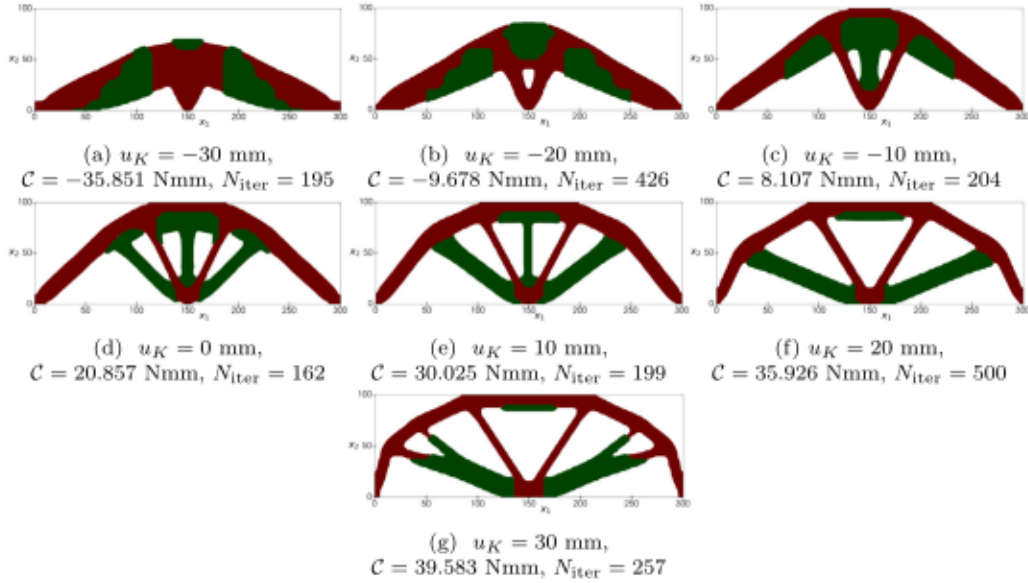


Fig. 11. BK2-2D: Optimised topologies solutions of problem (43) for different values of the applied displacement in the case of a bi-material structure.

in Figs. 11, 12 and 13, respectively. In each figure, results are provided in terms of the value of the generalised compliance C for the optimised solutions, of the number of iterations N_{iter} to achieve convergence and of the value of the applied displacement u_K . The optimised multi-material topologies illustrated in these figures are obtained by performing the threshold operation on the TF of each material phase at the end of the optimisation process: the threshold value of each material phase is calculated to satisfy the optimisation constraints of the considered problem formulation.

From the analysis of these results, one can infer the following remarks.

1. Regardless of the problem formulation, depending on the value of u_K , the generalised compliance can become negative, confirming, thus, the non-positive-definiteness of this functional under inhomogeneous Neumann–Dirichlet BCs.
2. For the three problem formulations, the value of u_K strongly influences the optimised distribution of materials M4 and M5. Specifically, when $u_K \geq 0$, the topology is strongly influenced by the applied force F_D and the TFs related to materials M4 and M5 evolve towards a truss-like configuration (at least for problems (43) and (44)) to minimise the displacement at point D (where the force F_D is applied). Conversely, when $u_K < 0$, the

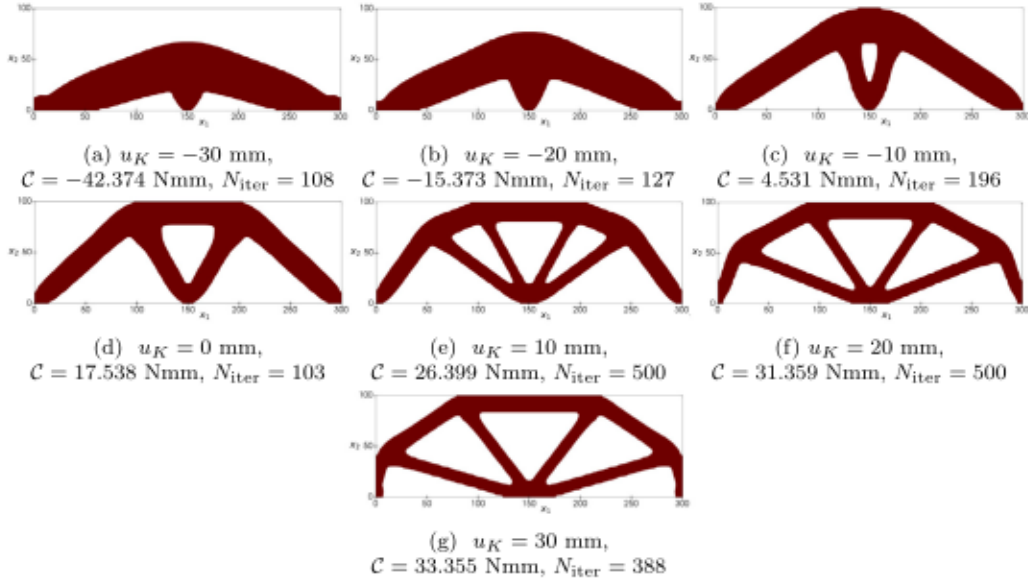


Fig. 12. BK2-2D: Optimised topologies solutions of problem (44) for different values of the applied displacement in the case of a bi-material structure.

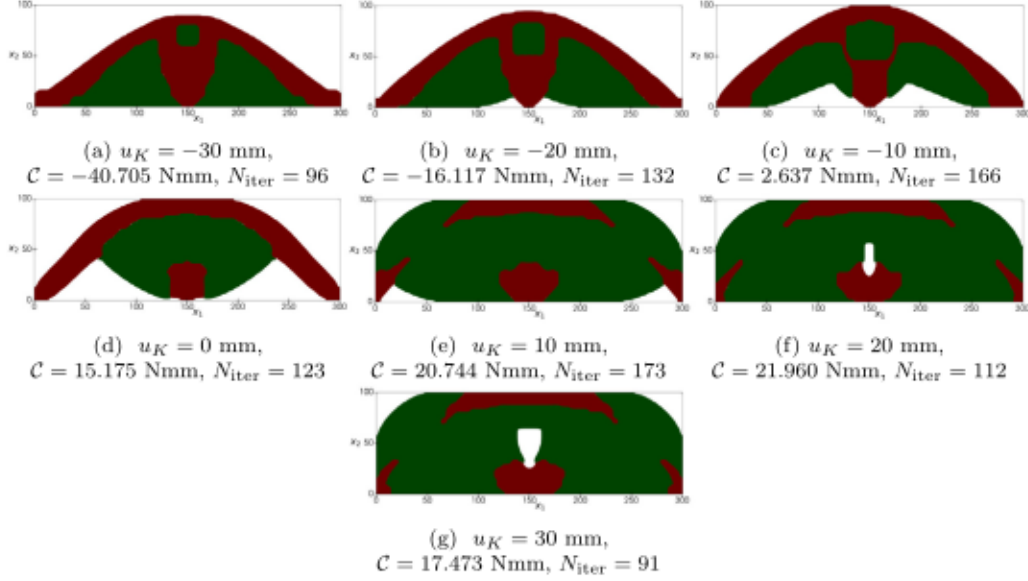


Fig. 13. BK2-2D: Optimised topologies solutions of problem (45) for different values of the applied displacement in the case of a bi-material structure.

topological descriptors of both material phases evolve towards a configuration tending to maximise the reaction at point K (where the displacement u_K is applied).

- When the CNLPP of Eq. (44) is considered, since the lightness requirement is imposed in terms of a constraint on the overall volume fraction of the structure, as expected, only the stiffest material phase, i.e., material M4, is kept within the design domain and its distribution is optimised in order to minimise the generalised compliance, as shown in Fig. 12.
- When comparing the optimised distribution of materials M4 and M5 solution of problem (43), shown in Fig. 11, to those solutions of problem (44), illustrated in Fig. 12, one can infer that, although the overall volume fraction occupied by the material phases in both solutions is the same, i.e., 40% of the volume of the design domain, the solutions shown in Fig. 12 are characterised by a value of the generalised compliance lower than the counterparts illustrated in Fig. 11 (for the same value

of u_K). This is an expected result because 15% of the volume of the design space is filled with material M5, which has a Young's modulus lower than the one of material M4. Indeed, as clearly shown in Fig. 11, material M5 is distributed over the regions of the structure characterised by lower values of the components of the stress tensor.

- As shown in Fig. 13, the optimised solutions of problem (45), wherein the lightness requirement is formulated in terms of a constraint on the overall mass fraction instead of a constraint on the overall volume fraction, are considerably different from those illustrated in Figs. 11 and 12. Particularly, since $M_{\text{ref}} = \rho_4 V_{\text{ref}}$, and $\gamma_V = \gamma_M = 0.4$ the optimised topologies illustrated in Figs. 12 and 13 are characterised by the same total mass, but not by the same overall volume because the density of material M5 is lower than the one of material M4 (i.e., $\frac{\rho_5}{\rho_4} = 0.3$). Moreover, in the optimised solutions of Fig. 13, although material M5 is less stiff than material M4, i.e., $\frac{E_5}{E_4} = 0.5$, this is

Table 5BK2-2D: reference value of the WAFD for different values of u_K and γ_{V_j} ($j = 1, 2$).

	$\gamma_{V_1} = 0.25, \gamma_{V_2} = 0.15$			$\gamma_{V_1} = 0.15, \gamma_{V_2} = 0.25$		
u_K [mm]	-30	0	30	-30	0	30
W_{ref} [Nmm]	686.81	686.27	686.81	1080.35	1080.01	1080.35

balanced by a higher volume of the material M5, which is used to considerably reduce the generalised compliance. Indeed, the optimised solutions illustrated in Fig. 13 are stiffer than those illustrated in Fig. 12 (for the same value of applied displacement u_K , except in the case $u_K = -30$ mm).

3.1.4. BK2-2D: work of applied forces and displacements minimisation under inhomogeneous Neumann–Dirichlet boundary conditions for bi-material structures

In this subsection, the CNLPP of Eq. (46) is solved for benchmark structure BK2-2D. The aim of this campaign of analyses is twofold. On the one hand, the influence of the inhomogeneous Neumann–Dirichlet BCs on the optimised distribution of the material phases for a continuum composed of two materials (i.e., materials M4 and M5 from Table 2), when the WAFD is considered as a cost function, is investigated. Particularly, problem (46) is solved for three values of the applied displacement, i.e., $u_K \in \{-30, 0, 30\}$ mm. On the other hand, the effect of the constraint on the volume fraction of each material phase on the optimised solution is studied. Specifically, two combinations of volume fractions of material phases M4 and M5 are considered (for each value of the imposed displacement u_K): in the first case they are set as $\gamma_{V_1} = 0.25$ (for M4) and $\gamma_{V_2} = 0.15$ (for M5), whilst in the second one they are chosen as $\gamma_{V_1} = 0.15$ (for M4) and $\gamma_{V_2} = 0.25$ (for M5).

In each case, the CNLPP of Eq. (46) is solved by considering a technological constraint related to the minimum fabricable dimension equal to $d_{MP} = 7$ mm (see Eq. (42)). According to the methodology presented in [46], this requirement can be satisfied by choosing a NURBS entity with the following integer parameters: $p_1 = p_2 = 4$ and $n_{CP} = 106 \times 34$.

An initial guess characterised by a uniform GF for both material phases, i.e., $\rho_j(\zeta_1, \zeta_2) = \hat{\rho}_j$ ($j = 1, 2$), has been considered for each analysis. Particularly, the value of $\hat{\rho}_j$ is calculated to satisfy the requirement on the volume fraction of the j th TF, i.e., $\Phi_j(\zeta_1, \zeta_2) = \gamma_{V_j}$.

Of course, the reference value of the WAFD W_{ref} depends upon the set of applied BCs and is reported in Table 5 for the different values of the applied displacement u_K and material volume fractions combination γ_{V_j} ($j = 1, 2$). The reference volume appearing in the CNLPP of Eq. (46) is $V_{ref} = a_1 a_2$. For each analysis the maximum number of iterations is $N_{iter}^{max} = 500$.

The optimised distribution of materials M4 (red colour) and M5 (green colour) solutions of problem (46) is illustrated in Fig. 14. In this figure, results are provided in terms of the value of the WAFD W for the optimised solutions, of the number of iterations N_{iter} to achieve convergence and of the value of the applied displacement u_K . Specifically, Fig. 14(a) illustrates the trend of W vs. u_K in the case $\gamma_{V_1} = 0.25, \gamma_{V_2} = 0.15$, whilst Fig. 14(b) shows the same curve in the case $\gamma_{V_1} = 0.15, \gamma_{V_2} = 0.25$. The optimised multi-material topologies illustrated in these figures are obtained by performing the threshold operation on the TF of each material phase at the end of the optimisation process: the threshold value of each material phase is calculated to satisfy the optimisation constraints of the considered problem formulation.

The following remarks can be drawn from the analysis of these results.

Consider the case wherein $\gamma_{V_1} = 0.25, \gamma_{V_2} = 0.15$. By comparing the optimised solutions of problem (46), shown in Fig. 14(a), to the optimised solutions of problem (43), illustrated in Figs. 11(a), 11(d) and 11(g), one can notice that the optimised distribution of materials

M4 and M5 is the same only in the case $u_K = 0$ mm, whilst they are considerably different when $u_K = -30$ mm and $u_K = 30$ mm. This is, indeed, an expected result: when $u_K = 0$ mm the generalised compliance and the WAFD coincide according to Eqs. (27) and (30). Conversely, when $u_K \neq 0$ mm, the optimised solution of problem (46) evolves towards a configuration minimising both the displacement at point D (where the force is applied) and the reaction at point K (where the displacement is applied). Indeed, regardless of the value of the imposed displacement u_K , the optimised solutions of problem (46) are characterised by an almost null reaction at point K, thus the value of the WAFD is practically constant and, accordingly, the optimised distribution of materials M4 and M5 is almost identical. The same remarks can be repeated for the case wherein $\gamma_{V_1} = 0.15, \gamma_{V_2} = 0.25$. Of course, the optimised distribution of materials M4 and M5 is not the same of the case wherein $\gamma_{V_1} = 0.25, \gamma_{V_2} = 0.15$. Moreover, in this case the distribution is weakly influenced by the value of imposed displacement: the optimised distribution of the stiffer material phase (M4) in the case $u_K = 0$ mm is not the same of the case $u_K \neq 0$ mm.

Finally, the trend of the WAFD vs. the iterations and the one of the maximum constraint vs. the iterations are reported in Fig. 15 for both combinations of γ_{V_1} and γ_{V_2} in the case $u_K = -30$ mm. As one can infer from these results, for both combinations of volume fractions, the optimised solution converges relatively fast, i.e., after less than 50 iterations when both optimisation constraints of Eq. (40) are active (almost equal to zero). However, the GCMMA algorithm does not stop the process because the stop criteria listed in Table 1 are not satisfied. Indeed, both calculations stop when the criterion on the difference between two consecutive values of the dimensionless cost function is satisfied: this occurs at iteration 496 in the case $\gamma_{V_1} = 0.25, \gamma_{V_2} = 0.15$, while it occurs at iteration 152 in the case $\gamma_{V_1} = 0.15, \gamma_{V_2} = 0.25$.

3.2. 3D benchmark structure

The geometry and the BCs of the 3D benchmark structure (BK3D) (taken from [59]) are shown in Fig. 16. The design domain is a parallelepiped with $a_1 = a_2 = 100$ mm and $a_3 = 60$ mm. The FE model is composed of $N_e = 40 \times 40 \times 24$ SOLID185 elements (i.e., solid elements with eight nodes and three DOFs per node, full integration scheme) submitted to the following BCs: (a) the nodes located at $x_1 = 0$ are clamped; (b) a point load $F_P = 1000$ N (along the x_3 axis) is applied on node P located at $(x_1, x_2, x_3) = (a_1, \frac{a_2}{2}, \frac{a_3}{2})$.

3.2.1. BK3D: application to a bi-material structure

The aim of the numerical analyses conducted on BK3D, in the case of bi-material solutions, is to investigate the influence of the problem formulation on the optimised distribution of materials within the design domain. Particularly, the materials M1 and M6 from Tables 2 and 3 are used in these analyses. To this purpose, problems (43) and (44) are solved by considering a technological constraint related to the minimum fabricable dimension equal to $d_{MP} = 7$ mm (see Eq. (42)). According to the methodology presented in [46], this requirement can be met by choosing a NURBS entity with $p_1 = p_2 = p_3 = 4$ and $n_{CP} = 24 \times 24 \times 16$.

For each problem formulation, an initial guess characterised by a uniform GF for both material phases, i.e., $\rho_j(\zeta_1, \zeta_2) = \hat{\rho}_j$, $j = 1, \dots, N_m$, has been considered for each analysis. Of course, the value of $\hat{\rho}_j$ for the j th material phase is the result of an iterative procedure conducted before the optimisation process that depends upon the problem formulation. Specifically, the value of $\hat{\rho}_j$ is calculated to meet: (a) the requirement on the volume fraction of the j th TF, i.e., $\Phi_j(\zeta_1, \zeta_2) = \gamma_{V_j}$ ($j = 1, 2$) for problem (43); (b) the requirement on the total volume fraction for problem (44). For each analysis, the maximum number of iterations is $N_{iter}^{max} = 500$.

Regarding problem (43), the volume fraction of materials M1 and M6 is set to $\gamma_{V_1} = 0.1$ and $\gamma_{V_2} = 0.2$, respectively, while, regarding problem (44), the overall volume fraction is set to $\gamma_V = 0.3$. It is

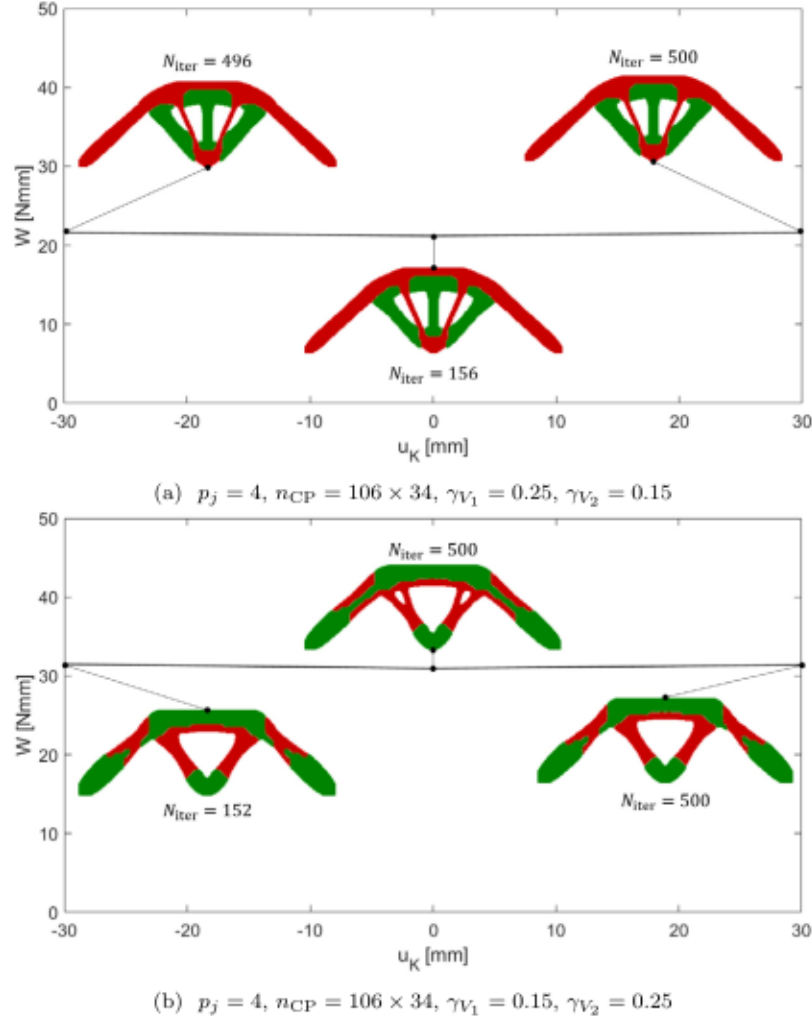


Fig. 14. BK2-2D: Optimised topologies solutions of problem (46) for different values of the applied displacement in the case of a bi-material structure.

noteworthy that the reference values of the generalised compliance (which coincides with the WAFD because $\mathbf{u}_{BC} = \mathbf{0}$) and of the volume for both problems (43) and (44) are the same, i.e., $V_{ref} = a_1 a_2 a_3$ and $C_{ref} = 2799.61 \text{ Nmm}$.

The optimised distribution of material M1 (red colour) and M6 (green colour) solutions of problems (43) and (44) is illustrated in Fig. 17. In this figure, the performances of the optimised solutions are provided in terms of the value of the generalised compliance C , of the overall volume and mass of the structure, i.e., V and M , respectively, as well as in terms of iterations N_{iter} to achieve convergence. The optimised multi-material topologies illustrated in Fig. 17 are obtained after the threshold operation on the TF of each material phase at the end of the optimisation process: the threshold value of each material phase is calculated to satisfy the optimisation constraints of the considered problem formulation.

The same remarks already done for the results discussed in Section 3.1.3 for 2D problems can be repeated here. It is noteworthy that, although the solutions of problems (43) and (44) are characterised by the same overall volume, the optimised topology solution of problem (43) is lighter than the one solution of problem (44) because the density of material M6 is lower than the one of material M1, i.e., $\frac{\rho_6}{\rho_1} = 0.23$. As expected, when the CNLPP of Eq. (44) is considered, since the lightness requirement is imposed in terms of a constraint on the overall volume fraction of the structure, only the material M1 is kept within the design domain and its distribution is optimised in order to minimise the generalised compliance, as shown in Fig. 17(b).

3.2.2. BK3D: application to a structure composed of three material phases

The CNLPP of Eq. (43) has been solved for BK3D by considering a structure composed of $N_m = 3$ material phases. The material properties used in this case are those of materials M1, M2 listed in Table 2 and material M6 from Table 3. Particularly, the TFs Φ_1 , Φ_2 and Φ_3 are associated to materials M1, M6, and M2, respectively. The volume fraction of materials M1, M2 and M6 is set to $\gamma_{V1} = \gamma_{V2} = \gamma_{V3} = 0.1$.

The minimum allowable dimension in Eq. (42) has been chosen equal to $d_{MP} = 7 \text{ mm}$. To satisfy this requirement without introducing explicit optimisation constraints [46], two cases are considered. In the first one, a B-spline entity characterised by $n_{CP} = 24 \times 24 \times 16$ and $p_1 = p_2 = p_3 = 2$ is used to describe the GFs. In the second case, a NURBS entity with $n_{CP} = 24 \times 24 \times 16$ and $p_1 = p_2 = p_3 = 4$ is employed. Both choices satisfy the constraint on the minimum length scale of Eq. (42).

Since $\mathbf{u}_{BC} = \mathbf{0}$, the generalised compliance and the WAFD coincide. An initial guess characterised by a uniform GF for each material phase, i.e., $\rho_j(\xi_1, \xi_2) = \hat{\rho}_j$, $j = 1, \dots, N_m$, has been considered for each analysis. The value of $\hat{\rho}_j$ for the j th material phase is the result of an iterative procedure conducted before the optimisation process: it is calculated to meet the requirement on the volume fraction of the j th TF, i.e., $\Phi_j(\xi_1, \xi_2) = \gamma_{V_j}$ ($j = 1, 2$). The reference value of the generalised compliance and of the volume are $C_{ref} = 4061.65 \text{ Nmm}$ and $V_{ref} = a_1 a_2 a_3$, whilst the maximum number of iterations is $N_{iter}^{max} = 500$.

Results are shown in Figs. 18 and 19, for B-spline and NURBS solutions, respectively, in terms of the TF Φ_j ($j = 1, \dots, N_m$) related to

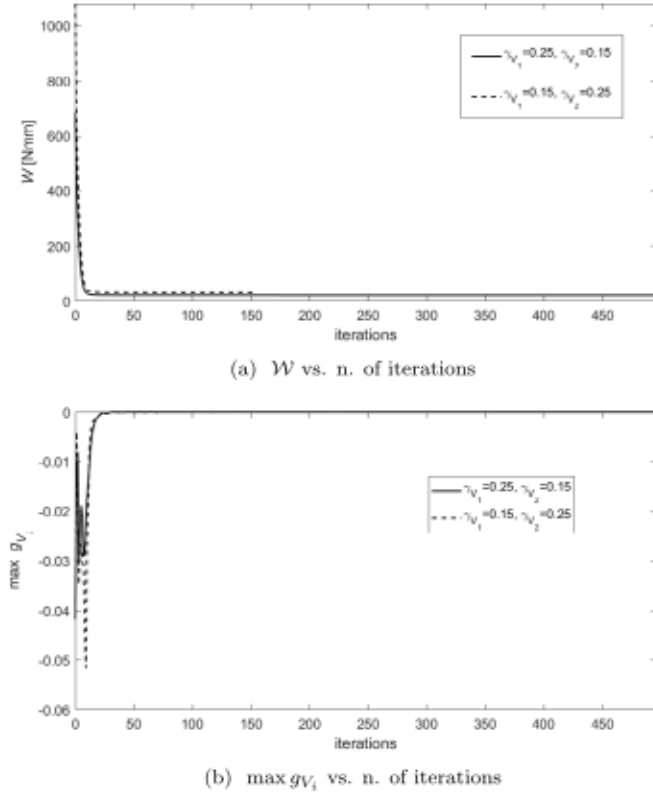


Fig. 15. BK2-2D: Trend of the cost function and of the maximum optimisation constraint vs. number of iterations of problem (46) for $u_K = -30$ mm in the case of a bi-material structure.

each material phase, of the optimised topology, of the related dimensionless generalised compliance $\frac{C}{C_{ref}}$ and of the number of iterations N_{iter} to achieve convergence. It is noteworthy that, for each case, the GCMMA algorithm stopped when the criterion on the difference between the objective function values of two consecutive iterations is met. Moreover, the optimised multi-material topologies illustrated in Figs. 18 and 19 are obtained after the (automatic) threshold operation on the TF of each material phase: M1, M2 and M6 are indicated in red, blue and green colours, respectively.

The remarks done for the results presented in Section 3.1.2 for 2D problems hold also in this case.

4. Conclusions

In this work, different aspects related to TO problems dealing with stiffness maximisation of multi-material structures under mixed inhomogeneous Neumann–Dirichlet BCs have been investigated.

Firstly, two different merit functions have been considered: the generalised compliance (which is related to the TPE of the structure) and the WAFD. Particularly, under inhomogeneous Neumann–Dirichlet BCs, the former provides a proper measure of the stiffness of the structure (and the related optimisation problem is self-adjoint), whilst the latter does not allow to quantify the structural stiffness and the associated optimisation problem is not self-adjoint. To the best of the authors' knowledge, the formal expression of the gradient of these response functions for MMTO problems under inhomogeneous Neumann–Dirichlet BCs have been derived for the first time and the main differences existing between the two formulations have been highlighted.

Secondly, the N-MMI scheme for MMTO problems has been correctly implemented without introducing further artificial filtering techniques and by taking advantage from the properties of general NURBS

hyper-surfaces. Due to the introduction of the weights among the design variables of the problem, at the end of the optimisation process the boundary of the material phases is smooth and clear (absence of superposition between materials and of intermediate values of the TF related to each material phase).

Thirdly, several numerical analyses have been performed to study the influence of the type of cost function, of the integer parameters involved in the definition of NURBS entity, of the number of material phases, of the elastic symmetry group of the generic material phase, of the applied BCs and of the type of lightness requirement on the optimised distribution of the materials within the structure.

Some features of the proposed method need to be highlighted.

1. As in the case of mono-material TO problems, the following advantages can be identified: (a) the optimised distribution of the material phases does not depend upon the mesh quality of the FE model because the GF of the generic material phase is described through a NURBS entity; however, the optimised solution is strongly influenced by integer parameters governing the shape of the NURBS entity; (b) no definition of artificial filters is required thanks to the local support property of NURBS entities; (c) the number of design variables is lower than classical density-based approaches wherein the pseudo-density field is defined element-wise; (d) the integration of geometrical constraints, like minimum and maximum length scale requirements, local curvature handling, overhang-angle requirement, into the problem formulation become a relatively easy task because, due to the utilisation of the NURBS entities, the boundary of the generic material phase is available at each iteration of the optimisation process.
2. As expected, the optimised distribution of the material phases solution of the problem involving the generalised compliance as a merit function is different from the optimised solution of the problem involving the WAFD as a merit function. Particularly, in the latter case, the optimised distribution of the material phases always converges towards a configuration minimising both the displacement of the nodes where external forces are applied and the reaction force of the nodes where non-zero displacement is imposed: this results in an optimised distribution of the material phases which is practically the same, regardless of the value of the imposed displacement. Conversely, when the generalised compliance is considered as objective function, the optimised solution is strongly influenced by the value of the applied displacement and converges always towards a configuration minimising the displacement of the nodes where external forces are applied and maximising the reaction force of the nodes where non-zero displacement is imposed.
3. The formulation of the lightness requirement has a strong influence on the optimised topology. Specifically, three different formulations have been considered: in the first case the lightness requirement is formulated as a constraint on the volume fraction of each material phase; in the second case it is formulated as a constraint on the overall volume fraction; in the third case it is formulated as a constraint on the overall mass. Depending on the adopted formulation, the optimised distribution of the material phases show significant variations and it is possible to access to local feasible minima characterised by outstanding properties in terms of structural stiffness and lightness.
4. The minimum member size requirement is handled implicitly by setting, before the optimisation process, the degrees of the Bernstein's polynomials and the number of CPs of the NURBS entity describing the GF of the generic material phase.

Regarding the prospects of this study, three potential research directions can be identified. Firstly, the formulation proposed here should be extended to the problem of the concurrent optimisation of the

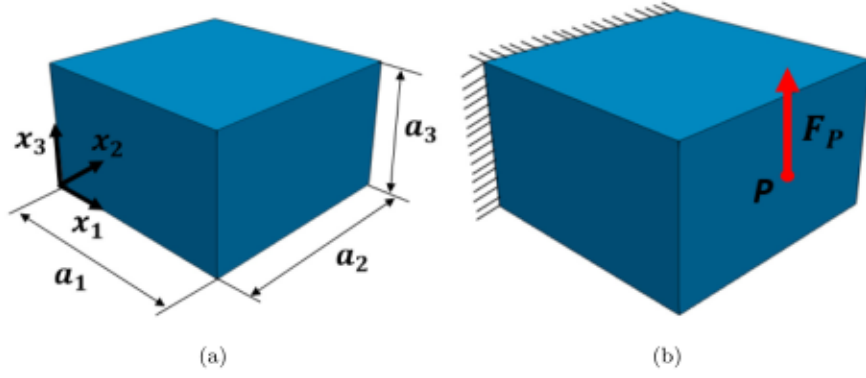


Fig. 16. (a) Geometry and (b) BCs of benchmark structure BK3D.

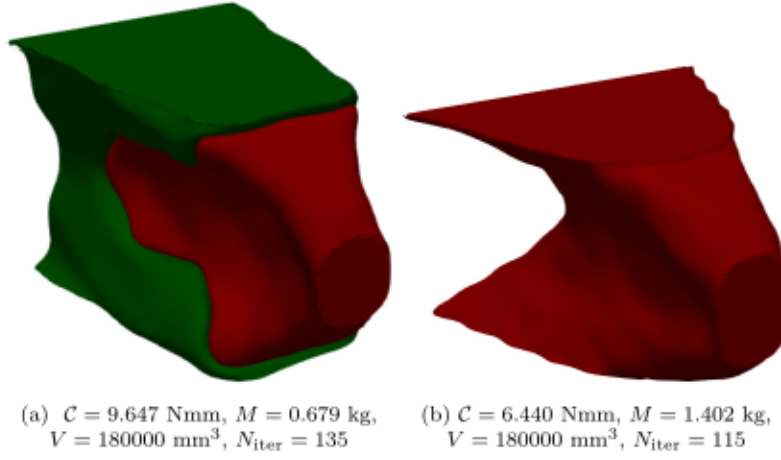


Fig. 17. BK3D: Optimised topologies solutions of problems (a) (43) and (b) (44) in the case of a bi-material structure.

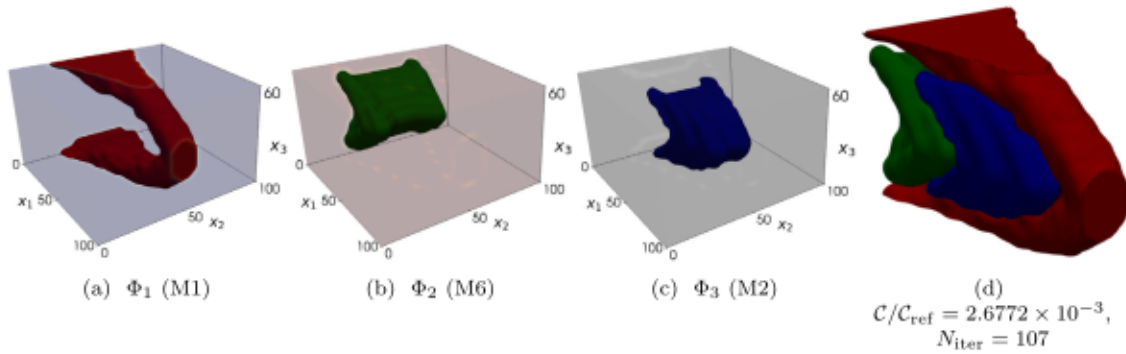


Fig. 18. BK3D: Optimised topology solution of problem (43) in the case of a structure composed of materials M1 (red), M2 (blue), and M6 (green), when using a B-spline entity with $n_{cp} = 24 \times 24 \times 16$ and $p_1 = p_2 = p_3 = 2$.

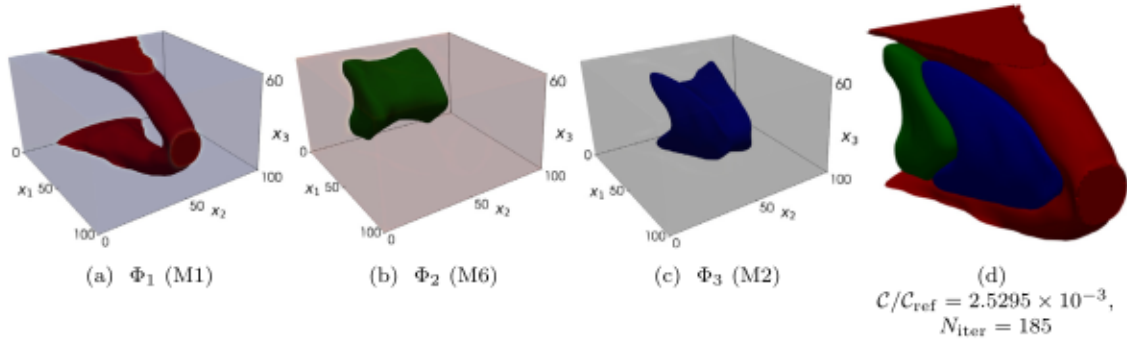


Fig. 19. BK3D: Optimised topology solution of problem (43) in the case of a structure composed of materials M1 (red), M2 (blue), and M6 (green), when using a NURBS entity with $n_{cp} = 24 \times 24 \times 16$ and $p_1 = p_2 = p_3 = 4$.

elastic symmetry group (in terms of shape and direction) and of the distribution within the design domain of the material phases under inhomogeneous Neumann–Dirichlet BCs.

Secondly, the theoretical/numerical framework should be extended to multi-physics analyses involving design requirements of different nature (e.g., structural, thermal, electromagnetic, etc.) to obtain multi-functional multi-material structures.

Finally, the approach should be generalised by integrating, on the one hand, the non-linear behaviour of the material (for each material phase) and, on the other hand, the behaviour of the interface together with suitable failure/delamination criteria.

CRediT authorship contribution statement

Marco Montemurro: Conceptualisation, Methodology, Software, Investigation, Validation, Writing – original draft, Writing – review & editing, Supervision, Funding acquisition. **Thibaut Rodriguez:** Methodology, Software, Investigation, Writing – original draft. **Jérôme Pailhès:** Writing – review & editing, Supervision. **Paul Le Texier:** Writing – review & editing, Supervision.

Declaration of competing interest

The authors declare that they have no known competing financial interests or personal relationships that could have appeared to influence the work reported in this paper.

Data availability

Data will be made available on request.

Acknowledgement

This work has been funded by Nouvelle-Aquitaine, France region through OCEAN-ALM project.

Appendix A. Gradient of the work of applied forces and displacements under mixed boundary conditions for multi-material structures

The proof of Proposition 2.1, provided here below, makes use of the adjoint method [60].

Proof. Under inhomogeneous Neumann–Dirichlet BCs, and by considering Eq. (16), the WAFD of Eq. (27) can be written as follows:

$$\mathcal{W} = \mathbf{f}^T \mathbf{u} + \mathbf{u}_{BC}^T \mathbf{r} + \boldsymbol{\eta}^T (\mathbf{K} \mathbf{u} + \mathbf{K}_{BC} \mathbf{u}_{BC} - \mathbf{f}) + \boldsymbol{\lambda}^T (\mathbf{K}_{BC}^T \mathbf{u} + \tilde{\mathbf{K}} \mathbf{u}_{BC} - \mathbf{r}), \quad (\text{A.1})$$

where $\boldsymbol{\eta} \in \mathbb{R}^{N_{DOF}}$ and $\boldsymbol{\lambda} \in \mathbb{R}^{N_{BC}}$ are two arbitrary vectors. Under the hypothesis that vectors \mathbf{f} and \mathbf{u}_{BC} do not depend on the TF of each material phase, i.e.,

$$\frac{\partial \mathbf{f}}{\partial \xi_{ik\tau}} = \mathbf{0}, \quad \frac{\partial \mathbf{u}_{BC}}{\partial \xi_{ik\tau}} = \mathbf{0}, \quad (\text{A.2})$$

the derivative of Eq. (A.1) reads:

$$\begin{aligned} \frac{\partial \mathcal{W}}{\partial \xi_{ik\tau}} &= \mathbf{f}^T \frac{\partial \mathbf{u}}{\partial \xi_{ik\tau}} + \mathbf{u}_{BC}^T \frac{\partial \mathbf{r}}{\partial \xi_{ik\tau}} + \\ &+ \boldsymbol{\eta}^T \left(\frac{\partial \mathbf{K}}{\partial \xi_{ik\tau}} \mathbf{u} + \mathbf{K} \frac{\partial \mathbf{u}}{\partial \xi_{ik\tau}} + \frac{\partial \mathbf{K}_{BC}}{\partial \xi_{ik\tau}} \mathbf{u}_{BC} \right) + \\ &+ \boldsymbol{\lambda}^T \left(\frac{\partial \mathbf{K}_{BC}^T}{\partial \xi_{ik\tau}} \mathbf{u} + \mathbf{K}_{BC}^T \frac{\partial \mathbf{u}}{\partial \xi_{ik\tau}} + \frac{\partial \tilde{\mathbf{K}}}{\partial \xi_{ik\tau}} \mathbf{u}_{BC} - \frac{\partial \mathbf{r}}{\partial \xi_{ik\tau}} \right). \end{aligned} \quad (\text{A.3})$$

In Eq. (A.3), vectors $\boldsymbol{\eta}$ and $\boldsymbol{\lambda}$ can be chosen such that the terms multiplying $\frac{\partial \mathbf{u}}{\partial \xi_{ik\tau}}$ and $\frac{\partial \mathbf{r}}{\partial \xi_{ik\tau}}$ vanish, i.e.,

$$\begin{aligned} \boldsymbol{\lambda} &= \mathbf{u}_{BC}, \\ \mathbf{K} \boldsymbol{\eta} &= -\mathbf{f} - \mathbf{K}_{BC} \boldsymbol{\lambda} = -\mathbf{f} - \mathbf{K}_{BC} \mathbf{u}_{BC} = \mathbf{K} \mathbf{u} - 2\mathbf{f}, \Rightarrow \boldsymbol{\eta} = \mathbf{u} - 2\mathbf{u}_0, \end{aligned} \quad (\text{A.4})$$

where \mathbf{u}_0 is the solution of Eq. (16) when BCs of Dirichlet's type are null, i.e., $\mathbf{u}_{BC} = \mathbf{0}$. By injecting Eq. (A.4) in Eq. (A.3) one obtains:

$$\begin{aligned} \frac{\partial \mathcal{W}}{\partial \xi_{ik\tau}} &= \mathbf{u}^T \frac{\partial \mathbf{K}}{\partial \xi_{ik\tau}} \mathbf{u} + 2\mathbf{u}^T \frac{\partial \mathbf{K}_{BC}}{\partial \xi_{ik\tau}} \mathbf{u}_{BC} + \mathbf{u}_{BC}^T \frac{\partial \tilde{\mathbf{K}}}{\partial \xi_{ik\tau}} \mathbf{u}_{BC} \\ &- 2\mathbf{u}_0^T \left(\frac{\partial \mathbf{K}}{\partial \xi_{ik\tau}} \mathbf{u} + \frac{\partial \mathbf{K}_{BC}}{\partial \xi_{ik\tau}} \mathbf{u}_{BC} \right) \\ &= \hat{\mathbf{u}}^T \frac{\partial \tilde{\mathbf{K}}}{\partial \xi_{ik\tau}} \hat{\mathbf{u}} - 2\mathbf{u}_0^T \left(\frac{\partial \mathbf{K}}{\partial \xi_{ik\tau}} \mathbf{u} + \frac{\partial \mathbf{K}_{BC}}{\partial \xi_{ik\tau}} \mathbf{u}_{BC} \right). \end{aligned} \quad (\text{A.5})$$

By considering the expression of the non-reduced stiffness matrix of Eq. (18) and by exploiting the local support property [42,44], the first term on the right-hand side of Eq. (A.5) can be simplified as:

$$\hat{\mathbf{u}}^T \frac{\partial \tilde{\mathbf{K}}}{\partial \xi_{ik\tau}} \hat{\mathbf{u}} = \alpha \sum_{e \in S_{kt}} \sum_{j=1}^{N_e} \Phi_{je}^{a-1} \frac{\partial \Phi_{je}}{\partial \rho_k} \frac{\partial \rho_{ke}}{\partial \xi_{ik\tau}} \hat{\mathbf{u}}^T \mathbf{L}_e^T \mathbf{K}_{je}^0 \mathbf{L}_e \hat{\mathbf{u}}. \quad (\text{A.6})$$

Considering Eq. (35), the above formula reads:

$$\hat{\mathbf{u}}^T \frac{\partial \tilde{\mathbf{K}}}{\partial \xi_{ik\tau}} \hat{\mathbf{u}} = \alpha \sum_{e \in S_{kt}} \frac{\partial \rho_{ke}}{\partial \xi_{ik\tau}} \mathbf{u}_e^T \mathbf{K}_{ke}^* \mathbf{u}_e, \quad (\text{A.7})$$

where $\mathbf{u}_e \in \mathbb{R}^{N_{DOF}^e}$ is the vector of generalised nodal displacements of element e according to Eq. (19).

The expressions of $\frac{\partial \mathbf{K}}{\partial \xi_{ik\tau}}$ and $\frac{\partial \mathbf{K}_{BC}}{\partial \xi_{ik\tau}}$ can be derived by applying Definition 2.1 to the derivative of Eq. (18) as follows:

$$\begin{aligned}\frac{\partial \hat{\mathbf{K}}}{\partial \xi_{ik\tau}} &= \alpha \sum_{e \in S_{k\tau}} \sum_{j=1}^{N_e} \Phi_{je}^{e-1} \frac{\partial \Phi_{je}}{\partial \rho_{ke}} \frac{\partial \rho_{ke}}{\partial \xi_{ik\tau}} \hat{\mathbf{L}}_e^T \mathbf{K}_{je}^0 \hat{\mathbf{L}}_e = \alpha \sum_{e \in S_{k\tau}} \frac{\partial \rho_{ke}}{\partial \xi_{ik\tau}} \hat{\mathbf{L}}_e^T \mathbf{K}_{ke}^* \hat{\mathbf{L}}_e, \\ \frac{\partial \mathbf{K}}{\partial \xi_{ik\tau}} &= \Re \left(\frac{\partial \hat{\mathbf{K}}}{\partial \xi_{ik\tau}}, \mathbf{I}_{BC}, \mathbf{I}_{BC} \right) \\ &= \alpha \sum_{e \in S_{k\tau}} \frac{\partial \rho_{ke}}{\partial \xi_{ik\tau}} \Re \left(\hat{\mathbf{L}}_e^T, \mathbf{I}_{BC}, \theta \right) \mathbf{K}_{ke}^* \Re \left(\hat{\mathbf{L}}_e, \theta, \mathbf{I}_{BC} \right), \\ \frac{\partial \mathbf{K}_{BC}}{\partial \xi_{ik\tau}} &= \Re \left(\frac{\partial \hat{\mathbf{K}}}{\partial \xi_{ik\tau}}, \mathbf{I}_{BC}, \mathbf{I}_U \right) \\ &= \alpha \sum_{e \in S_{k\tau}} \frac{\partial \rho_{ke}}{\partial \xi_{ik\tau}} \Re \left(\hat{\mathbf{L}}_e^T, \mathbf{I}_{BC}, \theta \right) \mathbf{K}_{ke}^* \Re \left(\hat{\mathbf{L}}_e, \theta, \mathbf{I}_U \right).\end{aligned}\quad (\text{A.8})$$

By taking into account for Eqs. (36) and (A.8), it is easy to check that the following equality holds:

$$\begin{aligned}\mathbf{u}_0^T \left(\frac{\partial \mathbf{K}}{\partial \xi_{ik\tau}} \mathbf{u} + \frac{\partial \mathbf{K}_{BC}}{\partial \xi_{ik\tau}} \mathbf{u}_{BC} \right) \\ = \alpha \sum_{e \in S_{k\tau}} \frac{\partial \rho_{ke}}{\partial \xi_{ik\tau}} \mathbf{u}_0^T \Re \left(\hat{\mathbf{L}}_e^T, \mathbf{I}_{BC}, \theta \right) \mathbf{K}_{ke}^* \\ \times \left[\Re \left(\hat{\mathbf{L}}_e, \theta, \mathbf{I}_{BC} \right) \mathbf{u} + \Re \left(\hat{\mathbf{L}}_e, \theta, \mathbf{I}_U \right) \mathbf{u}_{BC} \right] \\ = \alpha \sum_{e \in S_{k\tau}} \frac{\alpha}{\rho_e} \frac{\partial \rho_{ke}}{\partial \xi_{ik\tau}} \mathbf{u}_0^T \hat{\mathbf{L}}_e^T \mathbf{K}_{ke}^* \hat{\mathbf{L}}_e \mathbf{u} = \alpha \sum_{e \in S_{k\tau}} \frac{\partial \rho_{ke}}{\partial \xi_{ik\tau}} \mathbf{u}_{e0}^T \mathbf{K}_{ke}^* \mathbf{u}_e.\end{aligned}\quad (\text{A.9})$$

Finally, by injecting Eqs. (A.7) and (A.9) into Eq. (A.5), one can easily retrieve Eq. (34) and this last passage concludes the proof. ■

Appendix B. Gradient of the generalised compliance under mixed boundary conditions for multi-material structures

The proof of Proposition 2.2 is provided here below. Conceptually, it follows the same rationale used for the proof of Proposition 2.1.

Proof. Considering Eq. (16), the generalised compliance of Eq. (30) can be written as follows:

$$C = \mathbf{f}^T \mathbf{u} - \mathbf{u}_{BC}^T \mathbf{r} + \eta^T (\mathbf{K} \mathbf{u} + \mathbf{K}_{BC} \mathbf{u}_{BC} - \mathbf{f}) + \lambda^T (\mathbf{K}_{BC}^T \mathbf{u} + \tilde{\mathbf{K}} \mathbf{u}_{BC} - \mathbf{r}), \quad (\text{B.10})$$

where $\eta \in \mathbb{R}^{N_{\text{Dof}}}$ and $\lambda \in \mathbb{R}^{N_{\text{BC}}}$ are two arbitrary vectors. Under the hypothesis that vectors \mathbf{f} and \mathbf{u}_{BC} do not depend on the TFs, the derivative of Eq. (B.10) reads:

$$\begin{aligned}\frac{\partial C}{\partial \xi_{ik\tau}} &= \mathbf{f}^T \frac{\partial \mathbf{u}}{\partial \xi_{ik\tau}} - \mathbf{u}_{BC}^T \frac{\partial \mathbf{r}}{\partial \xi_{ik\tau}} + \\ &+ \eta^T \left(\frac{\partial \mathbf{K}}{\partial \xi_{ik\tau}} \mathbf{u} + \mathbf{K} \frac{\partial \mathbf{u}}{\partial \xi_{ik\tau}} + \frac{\partial \mathbf{K}_{BC}}{\partial \xi_{ik\tau}} \mathbf{u}_{BC} \right) + \\ &+ \lambda^T \left(\frac{\partial \mathbf{K}_{BC}^T}{\partial \xi_{ik\tau}} \mathbf{u} + \mathbf{K}_{BC}^T \frac{\partial \mathbf{u}}{\partial \xi_{ik\tau}} + \frac{\partial \tilde{\mathbf{K}}}{\partial \xi_{ik\tau}} \mathbf{u}_{BC} - \frac{\partial \mathbf{r}}{\partial \xi_{ik\tau}} \right).\end{aligned}\quad (\text{B.11})$$

In Eq. (B.11), vectors η and λ can be chosen such that the terms multiplying $\frac{\partial \mathbf{u}}{\partial \xi_{ik\tau}}$ and $\frac{\partial \mathbf{r}}{\partial \xi_{ik\tau}}$ vanish, i.e.

$$\begin{aligned}\lambda &= -\mathbf{u}_{BC}, \\ \mathbf{K} \eta &= -\mathbf{f} - \mathbf{K}_{BC} \lambda = -\mathbf{f} + \mathbf{K}_{BC} \mathbf{u}_{BC} = -\tilde{\mathbf{K}} \mathbf{u}_{BC} \Rightarrow \eta = -\mathbf{u}.\end{aligned}\quad (\text{B.12})$$

By injecting Eq. (B.12) in Eq. (B.11) and by considering Eq. (A.7) one obtains:

$$\begin{aligned}\frac{\partial C}{\partial \xi_{ik\tau}} &= -\mathbf{u}^T \frac{\partial \mathbf{K}}{\partial \xi_{ik\tau}} \mathbf{u} - 2\mathbf{u}^T \frac{\partial \mathbf{K}_{BC}}{\partial \xi_{ik\tau}} \mathbf{u}_{BC} - \mathbf{u}_{BC}^T \frac{\partial \tilde{\mathbf{K}}}{\partial \xi_{ik\tau}} \mathbf{u}_{BC} \\ &= -\hat{\mathbf{u}}^T \frac{\partial \hat{\mathbf{K}}}{\partial \xi_{ik\tau}} \hat{\mathbf{u}} = -\alpha \sum_{e \in S_{k\tau}} \frac{\partial \rho_{ke}}{\partial \xi_{ik\tau}} \mathbf{u}_e^T \mathbf{K}_{ke}^* \mathbf{u}_e,\end{aligned}\quad (\text{B.13})$$

which ends the proof. ■

References

- [1] J.-W. Choi, H.-C. Kim, R. Wicker, Multi-material stereolithography, *J. Mater. Process. Technol.* 211 (3) (2011) 318–328.
- [2] R. Singh, R. Kumar, I. Farina, F. Colangelo, L. Feo, F. Fraternali, Multi-material additive manufacturing of sustainable innovative materials and structures, *Polymers* 11 (1) (2019) <http://dx.doi.org/10.3390/polym11010062>.
- [3] A. Muguruza, J.B. Bo, A. Gómez, J. Minguella-Canela, J. Fernandes, F. Ramos, E. Xuriguera, A. Varea, A. Cirera, Development of a multi-material additive manufacturing process for electronic devices, *Procedia Manuf.* 13 (2017) 746–753, Manufacturing Engineering Society International Conference 2017, MESIC 2017, 28–30 June 2017, Vigo (Pontevedra), Spain.
- [4] C.F. Tey, X. Tan, S.L. Sing, W.Y. Yeong, Additive manufacturing of multiple materials by selective laser melting: Ti-alloy to stainless steel via a Cu-alloy interlayer, *Addit. Manuf.* 31 (2020) 100970, <http://dx.doi.org/10.1016/j.addma.2019.100970>.
- [5] A. Reichardt, R.P. Dillon, J.P. Borgonia, A.A. Shapiro, B.W. McEnerney, T. Momose, P. Hosemann, Development and characterization of Ti-6Al-4V to 304L stainless steel gradient components fabricated with laser deposition additive manufacturing, *Mater. Des.* 104 (2016) 404–413.
- [6] Y.-H. Chueh, X. Zhang, J.C.-R. Ke, Q. Li, C. Wei, L. Li, Additive manufacturing of hybrid metal/polymer objects via multiple-material laser powder bed fusion, *Addit. Manuf.* 36 (2020) 101465, <http://dx.doi.org/10.1016/j.addma.2020.101465>.
- [7] R. Matsuzaki, T. Kanatani, A. Todoroki, Multi-material additive manufacturing of polymers and metals using fused filament fabrication and electroforming, *Addit. Manuf.* 29 (2019) 100812, <http://dx.doi.org/10.1016/j.addma.2019.100812>.
- [8] M.P. Bendsoe, Optimal shape design as a material distribution problem, *Struct. Optim.* 1 (4) (1989) 193–202.
- [9] M. Bendsoe, N. Kikuchi, Generating optimal topologies in structural design using a homogenization method, *Comput. Methods Appl. Mech. Engrg.* 71 (1988) 197–224.
- [10] M. Bendsoe, O. Sigmund, *Topology Optimization - Theory, Methods and Applications*, Springer-Verlag Berlin Heidelberg, 2004.
- [11] G. Agrawal, A. Gupta, R. Chowdhury, A. Chakrabarti, Robust topology optimization of negative Poisson's ratio metamaterials under material uncertainty, *Finite Elem. Anal. Des.* 198 (2022) 103649, URL <https://www.sciencedirect.com/science/article/pii/S0168874X21001311>.
- [12] Topology optimization for transient response problems involving thermoelastic materials, *Finite Elem. Anal. Des.* 201 (2022) 103695, URL <https://www.sciencedirect.com/science/article/pii/S0168874X21001694>.
- [13] J. Sethian, *Level Set Methods and Fast Marching Methods - Evolving interfaces in computational geometry, fluid mechanics, computer vision, and materials science*, Cambridge University Press, 1999.
- [14] G. Allaire, F. Jouve, A.-M. Toader, Structural optimization using sensitivity analysis and a level-set method, *J. Comput. Phys.* 194 (1) (2004) 363–393.
- [15] M.Y. Wang, X. Wang, D. Guo, A level set method for structural topology optimization, *Comput. Methods Appl. Mech. Engrg.* 192 (1) (2003) 227–246.
- [16] M. de Ruiter, F. van Keulen, Topology optimization using a topology description function, *Struct. Multidiscip. Optim.* 26 (6) (2004) 406–416.
- [17] T. Miki, S. Nishiwaki, Topology optimization of the support structure for heat dissipation in additive manufacturing, *Finite Elem. Anal. Des.* 203 (2022) 103708, URL <https://www.sciencedirect.com/science/article/pii/S0168874X21001803>.
- [18] Y. Xie, G. Steven, A simple evolutionary procedure for structural optimization, *Comput. Struct.* 49 (5) (1993) 885–896.
- [19] X. Yang, Y. Xie, G. Steven, O. Querin, Bidirectional evolutionary method for stiffness optimization, *AIAA J.* 37 (1999) 1483–1488.
- [20] R.L. Pereira, H.N. Lopes, R. Pavanetto, Topology optimization of acoustic systems with a multiconstrained BESO approach, *Finite Elem. Anal. Des.* 201 (2022) 103701, URL <https://www.sciencedirect.com/science/article/pii/S0168874X21001736>.
- [21] O. Sigmund, S. Torquato, Design of materials with extreme thermal expansion using a three-phase topology optimization method, *J. Mech. Phys. Solids* 45 (6) (1997) 1037–1067.
- [22] M.P. Bendsoe, O. Sigmund, Material interpolation schemes in topology optimization, *Arch. Appl. Mech.* 69 (9) (1999) 635–654.
- [23] T. Gao, W. Zhang, Topology optimization of multiphase material structures under design dependent pressure loads, *Int. J. Simul. Multidiscip. Des. Optim.* 3 (2009) 297–306.
- [24] G. Vantighem, V. Boel, M. Steeman, W. Corte, Multi-material topology optimization involving simultaneous structural and thermal analyses, *Struct. Multidiscip. Optim.* 59 (2019) 731–743.
- [25] A. Takezawa, M. Kobashi, Design methodology for porous composites with tunable thermal expansion produced by multi-material topology optimization and additive manufacturing, *Composites B* 131 (2017) 21–29.
- [26] C. Li, I.Y. Kim, Multi-material topology optimization for automotive design problems, *Proc. Inst. Mech. Eng. D* 232 (14) (2017) 1950–1969.
- [27] L. Gibiansky, O. Sigmund, Multiphase composites with extremal bulk modulus, *J. Mech. Phys. Solids* 48 (2000) 461–498.

- [28] O. Sigmund, Design of multiphysics actuators using topology optimization – Part II: Two-material structures, *Comput. Methods Appl. Mech. Engrg.* 190 (49) (2001) 6605–6627.
- [29] W. Zuo, K. Saitou, Multi-material topology optimization using ordered SIMP interpolation, *Struct. Multidiscip. Optim.* 55 (2017) 477–491.
- [30] J. Stegmann, E. Lund, Discrete material optimization of general composite shell structures, *Internat. J. Numer. Methods Engrg.* 62 (14) (2005) 2009–2027.
- [31] E. Lund, J. Stegmann, On structural optimization of composite shell structures using a discrete constitutive parametrization, *Wind Energy* 8 (1) (2005) 109–124.
- [32] C. Hvejsel, E. Erik, Material interpolation schemes for unified topology and multi-material optimization, *Struct. Multidiscip. Optim.* 43 (2011) 811–825.
- [33] C. Hvejsel, E. Lund, M. Stolpe, Optimization strategies for discrete multi-material stiffness optimization, *Struct. Multidiscip. Optim.* 44 (2011) 149–163.
- [34] T. Gao, W. Zhang, A mass constraint formulation for structural topology optimization with multiphase materials, *Internat. J. Numer. Methods Engrg.* 88 (2011) 774–796.
- [35] J. Gao, Z. Luo, M. Xiao, L. Gao, P. Li, A NURBS-based Multi-Material Interpolation (N-MMI) for isogeometric topology optimization of structures, *Appl. Math. Model.* 81 (2020) 818–843.
- [36] R. Franke, Scattered data interpolation: Tests of some methods, *Math. Comp.* 38 (1982) 181–200.
- [37] M.Y. Wang, X. Wang, “Color” level sets: a multi-phase method for structural topology optimization with multiple materials, *Comput. Methods Appl. Mech. Engrg.* 193 (6) (2004) 469–496.
- [38] S. Chu, L. Gao, M. Xiao, Z. Luo, H. Li, Stress-based multi-material topology optimization of compliant mechanisms, *Internat. J. Numer. Methods Engrg.* 113 (7) (2018) 1021–1044.
- [39] S. Chu, M. Xiao, L. Gao, H. Li, A level set-based method for stress-constrained multimaterial topology optimization of minimizing a global measure of stress, *Internat. J. Numer. Methods Engrg.* 117 (7) (2019) 800–818.
- [40] Y. Wang, Z. Luo, Z. Kang, N. Zhang, A multi-material level set-based topology and shape optimization method, *Comput. Methods Appl. Mech. Engrg.* 283 (2015) 1570–1586.
- [41] J. Liu, Y. Ma, A new multi-material level set topology optimization method with the length scale control capability, *Comput. Methods Appl. Mech. Engrg.* 329 (2018) 444–463.
- [42] M. Montemurro, On the structural stiffness maximisation of anisotropic continua under inhomogeneous Neumann-Dirichlet boundary conditions, *Compos. Struct.* 287 (2022) 115289, <http://dx.doi.org/10.1016/j.compstruct.2022.115289>.
- [43] G. Costa, M. Montemurro, J. Pailhès, A 2D topology optimisation algorithm in NURBS framework with geometric constraints, *Int. J. Mech. Mater. Des.* 14 (4) (2018) 669–696.
- [44] G. Costa, M. Montemurro, J. Pailhès, NURBS Hypersurfaces for 3D Topology Optimisation Problems, *Mech. Adv. Mater. Struct.* 28 (7) (2021) 665–684.
- [45] T. Rodriguez, M. Montemurro, P. Le Texier, J. Pailhès, Structural displacement requirement in a topology optimization algorithm based on isogeometric entities, *J. Optim. Theory Appl.* 184 (2020) 250–276.
- [46] G. Costa, M. Montemurro, J. Pailhès, Minimum Length Scale Control in a NURBS-based SIMP Method, *Comput. Methods Appl. Mech. Engrg.* 354 (2019) 63–989.
- [47] G. Costa, M. Montemurro, J. Pailhès, N. Perry, Maximum length scale requirement in a topology optimisation method based on NURBS hyper-surfaces, *CIRP Annals* 68 (1) (2019) 153–156.
- [48] G. Costa, M. Montemurro, Eigen-frequencies and harmonic responses in topology optimisation : a CAD-compatible algorithm, *Eng. Struct.* 214 (2020) 110602.
- [49] M. Montemurro, K. Refai, A topology optimization method based on non-uniform rational basis spline hyper-surfaces for heat conduction problems, *Symmetry* 13 (5) (2021) 888.
- [50] M. Montemurro, G. Bertolino, T. Roiné, A general multi-scale topology optimisation method for lightweight lattice structures obtained through additive manufacturing technology, *Compos. Struct.* 258 (2021) 113360.
- [51] T. Roiné, M. Montemurro, J. Pailhès, Stress-based topology optimization through non-uniform rational basis spline hyper-surfaces, *Mech. Adv. Mater. Struct.* 29 (23) (2022) 3387–3407.
- [52] G. Bertolino, M. Montemurro, Two-scale topology optimisation of cellular materials under mixed boundary conditions, *Int. J. Mech. Sci.* 216 (2022) 106961.
- [53] M. Montemurro, K. Refai, A. Catapano, Thermal design of graded architected cellular materials through a CAD-compatible topology optimisation method, *Compos. Struct.* 280 (2022) 114862.
- [54] G. Costa, M. Montemurro, J. Pailhès, A general hybrid optimization strategy for curve fitting in the non-uniform rational basis spline framework, *J. Optim. Theory Appl.* 176 (1) (2017) 225–251.
- [55] G. Bertolino, M. Montemurro, N. Perry, F. Pourroy, An efficient hybrid optimisation strategy for surface reconstruction, *Comput. Graph. Forum* 40 (6) (2021) 215–241.
- [56] L. Piegl, W. Tiller, *The NURBS Book*, Springer-Verlag, Berlin, Heidelberg, New York, 1997.
- [57] Z. Hashin, S. Shtrikman, A variational approach to the theory of the elastic behaviour of multiphase materials, *J. Mech. Phys. Solids* 11 (1963) 127–140.
- [58] K. Svanberg, A class of globally convergent optimization methods based on conservative convex separable approximations, *SIAM. Optim.* 12 (2002) 555–573.
- [59] D. Li, I. Kim, Multi-material topology optimization for practical lightweight design, *Struct. Multidiscip. Optim.* 58 (2018) 1081–1094.
- [60] R.M. Errico, What is an adjoint model? *Bull. Am. Meteorol. Soc.* 78 (11) (1997) 2577–2592.